

ANALYSIS AND DESIGN OF A FLUIDIC-RECONFIGURABLE SUBSTRATE
INTEGRATED WAVEGUIDE RESONATOR

A Thesis

by

JOEL DANIEL BARRERA

Submitted to the Office of Graduate Studies of
Texas A&M University
in partial fulfillment of the requirements for the degree of
MASTER OF SCIENCE

December 2011

Major Subject: Electrical Engineering

Analysis and Design of a Fluidic-Reconfigurable Substrate Integrated Waveguide

Resonator

Copyright 2011 Joel Daniel Barrera

ANALYSIS AND DESIGN OF A FLUDIC-RECONFIGURABLE SUBSTRATE
INTEGRATED WAVEGUIDE RESONATOR

A Thesis

by

JOEL DANIEL BARRERA

Submitted to the Office of Graduate Studies of
Texas A&M University
in partial fulfillment of the requirements for the degree of

MASTER OF SCIENCE

Approved by:

Chair of Committee,	Gregory H. Huff
Committee Members,	Robert Nevels
	Harlan Harris
	Raktim Bhattacharya
Head of Department,	Costas Georghiades

December 2011

Major Subject: Electrical Engineering

ABSTRACT

Analysis and Design of a Fluidic-Reconfigurable Substrate Integrated Waveguide
Resonator. (December 2011)

Joel Daniel Barrera, B.S., Texas A&M University

Chair of Advisory Committee: Dr. Gregory H. Huff

Microwave filters play key roles in controlling the frequency response at specific locations of any communications, radar, or test system. Microwave resonators provide the frequency selective building blocks necessary for filter design. Reconfigurable/tunable microwave resonators have facilitated the design of tunable filters. Recently, MEMS based tuning mechanisms developed widely tunable resonators maintaining high Q ; however, limit in the number of reconfiguration states.

This thesis proposes a fluidic-reconfigurable X-band SIW resonator capable of continuous tunability across the reconfiguration range. A dielectric post of fluidic dispersions with variable material properties embedded in a two inductive post static SIW resonator defines the tuning mechanism. The development of an analytical closed-form expression for the resonant frequency and Q across reconfiguration, a circuit model, and full-wave simulation predicts the tunable performance with estimated material properties of the fluidic dispersion. Measured data on an initial tunable SIW resonator design showed good reconfiguration performance but more losses than expected which could potentially be explained from the discovery of a major design

error not associated with the resonator itself. A second tunable SIW resonator designed and fabricated proves the material properties of the fluidic dispersions contain more losses than estimated and hinder the resonators performance. By comparing simulated and measured data new estimates for the material properties of the fluidic dispersion are proposed which agree with trends in recent literature. Low-loss fluidic dispersions will enable a significant performance increase in the current tunable SIW resonator. Two low-cost material measurement systems are designed to expedite research efforts in finding low-loss microwave fluidics. Both systems accurately compute dielectric constant but not loss tangents. The initial systems provide necessary first steps in the design of future highly accurate material measurement systems.

DEDICATION

This thesis is dedicated to my grandparents Rosa & Octavio Guajardo and Socorro & Hector Barrera.

ACKNOWLEDGEMENTS

I would like to thank my committee chair, Dr. Huff, for his guidance and support throughout the course of this research. I would also like to thank my committee members Dr. Nevels, Dr. Harris, and Dr. Bhattacharya for taking the time to critic this work.

Thanks also go to my friends and colleagues and the department faculty and staff for making my time at Texas A&M University a great experience. I also want to extend my gratitude to the Louis Stokes Alliance for Minority Participation Bridge-to-the-Doctorate fellowship program for providing funding during the duration of my M.S.

Finally, thanks to my mother and father for their love and encouragement.

NOMENCLATURE

CF-MMS	Coaxial fixture material measurement system
DRA	Dielectric resonator antenna
FS-MMS	Free-space material measurement system
MG	Maxwell-Garnett
MMS	Material measurement system
MUT	Material under test
PNA	Programmable network analyzer
SIW	Substrate integrated waveguide
SGH	Standard gain horn
RWG	Rectangular waveguide
TE	Transverse electric
TL	Transmission line
TEM	Transvers electric and magnetic
TM	Transverse magnetic

TABLE OF CONTENTS

	Page
ABSTRACT	iii
DEDICATION	v
ACKNOWLEDGEMENTS	vi
NOMENCLATURE	vii
TABLE OF CONTENTS	viii
LIST OF FIGURES	x
LIST OF TABLES	xiv
CHAPTER	
I INTRODUCTION	1
II BACKGROUND	4
2.1 Network Analysis	4
2.2 Substrate Integrated Waveguides	7
2.3 Microwave Resonators	11
2.4 Cavity Material Perturbations	14
2.5 Maxwell-Garnett Mixing Rule	15
2.6 Coupled Resonator Filters	16
III ANALYSIS	18
3.1 The Static SIW Resonator	18
3.2 Reconfiguration Mechanism	22
IV DESIGN ITERATION 1	29
4.1 Initial Dispersions	29
4.2 Predicted Performance	30
4.3 Fabrication and Measured Results	34

CHAPTER	Page
V DESIGN ITERATION 2	38
5.1 Design Changes	38
5.2 New Dispersions	40
5.3 Predicted Performance	40
5.4 Fabrication and Measured Results	43
5.5 Material Property Study	45
5.6 Discussion and Conclusion	51
VI MATERIAL MEASUREMENTS.....	54
6.1 Overview	54
6.2 Initial Low Cost Test Fixtures.....	56
6.3 Calculation of Complex Dielectric Constant	59
6.4 Data Processing	64
6.5 Free-Space MMS Initial Testing	65
6.6 Free-Space MMS Small Sample Testing	67
6.7 Coaxial Fixture MMS Initial Testing	68
6.8 Conclusion.....	70
VII FUTURE WORK AND CONCLUSION	71
7.1 A Tunable Two-Pole Chebyshev SIW Filter	71
7.2 Possible 3 rd SIW Tunable Resonator Design Iterations	72
7.3 Advancements to MMS.....	74
7.4 Final Conclusion	74
REFERENCES.....	76
APPENDIX A	79
APPENDIX B	82
VITA	89

LIST OF FIGURES

FIGURE		Page
1	Two-port network showing network variables.....	4
2	Useful two-port networks and their $ABCD$ parameters.....	5
3	Geometry of a conventional rectangular waveguide (RWG).....	7
4	Geometry of a substrate integrated waveguide (SIW).	8
5	Tapered transition between a 50Ω microstrip line and SIW.	11
6	Geometry of a conventional rectangular resonant cavity.	11
7	Cavity material perturbation theory (a) original cavity and (b) perturbed cavity.....	14
8	Maxwell-Garnett mixing rule for fluidic dispersions utilizing spherical (red), needle (blue), and disc (green) particles.	15
9	n -pole coupled-resonator filter circuit.....	16
10	Narrowband bandpass filter Chebyshev response.....	17
11	The static SIW resonator.	18
12	Conceptual circuit model for the static SIW resonator.	18
13	Advanced circuit model for the static SIW resonator.	19
14	Equivalent cavity for the static SIW resonator.....	21
15	The tunable SIW resonator with the fluidic dispersion (red).	22
16	Conceptual circuit model for the tunable SIW resonator.	22
17	Advanced circuit model for the tunable SIW resonator.	23
18	Cavity material perturbation model for the tunable SIW resonator.	25

FIGURE	Page
19 BSTO used for initial dispersions with an SEM image.	29
20 Complete HFSS simulation model for the initial tunable SIW resonator. .	31
21 Circuit model (dotted) and HFSS simulation (solid) predicted S11 response for the initial tunable SIW resonator.	32
22 Circuit model (dotted) and HFSS simulation (solid) predicted S21 response for the initial tunable SIW resonator.	32
23 Measured (solid) and HFSS simulation (dotted) S11 response for the initial tunable SIW resonator.	36
24 Measured (solid) and HFSS simulation (dotted) S21 response for the initial tunable SIW resonator.	36
25 Capacitive loading effected from the SMA connectors indicated by red arrows.	37
26 Complete HFSS simulation model for the 2 nd SIW tunable resonator.	39
27 Circuit model (dotted) and HFSS simulation (solid) predicted S11 response for the 2nd tunable SIW resonator.	41
28 Circuit model (dotted) and HFSS simulation (solid) predicted S21 response for the 2nd tunable SIW resonator.	41
29 Measured (solid) and HFSS simulated (dotted) S11 response for the 2nd tunable SIW resonator.	44
30 Measured (solid) and HFSS simulated (dotted) S21 response for the 2nd tunable SIW resonator.	44
31 HFSS simulated S_{11} response for the SF loss tangent parametric study. ...	46
32 HFSS simulated S_{21} response for the SF loss tangent parametric study. ...	46
33 Measured (solid) and HFSS simulated (dotted) S11 response for the 2nd tunable SIW resonator with new estimated fluidic dispersion permittivity.	48

FIGURE	Page
34 Measured (solid) and HFSS simulated (dotted) S21 response for the 2nd tunable SIW resonator with new estimated fluidic dispersion permittivity.....	48
35 Measured (solid) and circuit model (dotted) S11 response for the 2nd tunable SIW resonator with new estimated fluidic dispersion permittivity.....	50
36 Measured (solid) and circuit model (dotted) S21 response for the 2nd tunable SIW resonator with new estimated fluidic dispersion permittivity.....	50
37 Commercially available MMSs.....	55
38 CF-MMS for measuring liquid samples.....	56
39 Assembly procedure for the CF-MMS.....	57
40 FS-MMS capable of measuring solids and semi-solid materials.	58
41 Radiation characteristics of a SGH antenna.....	58
42 Block diagram for the MMSs.....	59
43 Diagram of incidence, reflection, and transmission from the MUT and TL equivalent circuit.....	60
44 Signal flow graph formulation for the reflections and transmissions off the MUT boundaries.....	61
45 Decomposed signal flow graph for the reflections and transmissions off the MUT boundaries.....	61
46 Complete reflection and transmission diagram off and through the MUT.	63
47 Block diagram of the data processing code.....	64
48 Large Plexiglas sample measurement results using the FS-MMS.	66
49 Small Plexiglas sample measurement results using the FS-MMS.	67

FIGURE		Page
50	Small Plexiglas sample measurement results using the FS-MMS with a small sample MUT holder.....	68
51	Air sample measurement results using the CF-MMS.	69
52	SF sample measurement results using the CF-MMS.	70
53	A Two-pole tunable SIW Chebyshev filter.....	71
54	Attempts at possible 3rd tunable SIW resonator design iterations.....	73

LIST OF TABLES

TABLE		Page
1	Limits and physical interpretations of two-port S parameters.....	6
2	Estimated ε_d for initial fluidic dispersions using the MG mixing rule.....	30
3	Dimensions of the initial tunable SIW resonator	31
4	Summary of $f_{0,g}$ and Q for the initial tunable SIW resonator design.	34
5	Dimensions of the 2nd tunable SIW resonator.....	39
6	Estimated ε_d for 2nd batch of fluidic dispersions using the MG mixing rule.	40
7	Summary of $f_{0,g}$ and Q for the 2nd tunable SIW resonator design.....	43
8	New predicted ε_d for new estimated ε_1 and ε_2 using the MG mixing rule.	47
9	Predicted tunable SIW resonator Q with new estimated fluidic dispersion permittivity.	51
10	Tunable SIW resonator dissipation α with the new estimated fluidic dispersion permittivity.....	52

CHAPTER I

INTRODUCTION

Microwave filters characterize the frequency response at specified locations in a microwave system. Typical responses include lowpass, highpass, bandpass, and bandstop. Communication, radar, and test and measurement systems utilized microwave filters as essential building blocks providing proper system functionality. Coupled-resonators are [provide] excellent circuit components for narrowband bandpass filter design. A general technique for designing coupled-resonator filters regardless of resonator topology has been developed and presented well in [1]. Waveguide resonators capable of achieving very high quality factors ($Q > 1000$) offer exceptional performance for such applications [2]. Due to bulk and weight, regular waveguides become cumbersome in system integration for reduction in design space and system weight.

In the past decade, substrate integrated waveguides (SIWs) have adapted traditional waveguide designs into planar form providing a low-cost, low-profile alternative to regular waveguides [3, 4]. The lateral walls of the regular waveguide guide are replaced by rows of periodic vias within a substrate. The dielectric filling the SIW decreases the Q of an SIW resonator compared to an air filled regular waveguide resonator from 1000s to 100s. However, coupled-resonator SIW filters exhibiting exceptional performance have been designed in [5-7].

This thesis follows the style of *IEEE Transactions on Microwave Theory and Techniques*.

The interest in frequency agile and wideband systems such as software defined radios [8], flexible transceivers, and multiband communications systems leads to a direct interest in reconfigurable/tunable microwave filters. Channel separation realized through tunable narrowband filters increases the feasibility of future multiband communications systems [9]. Tunable filters replace complex filter-banks consisting of numerous switches and fixed filters, reducing the front end cost, footprint, and insertion loss for software defined radios and flexible transceivers [10]. At the heart of most reconfigurable filters are tunable resonators. When coupled together, tunable resonators create filters capable of manipulating performance across the frequency spectrum.

Microstrip resonators loaded with integrated microelectromechanical system (MEMS) capacitive switches for tunable filters have been studied in [10-12]. Recently, packaged MEMS switches have successfully created tunable SIW resonators in [13]. Tuning ranges from 14 % in [11] to 32% in [10] have been achieved while maintaining high resonator quality factors (100s). RF MEMS clearly offer attractive solutions for tunable microwave resonators and filters; however, are limited to a fixed number for reconfiguration states across the tunable range. Including more reconfigurations states increases the number of MEMS switches increasing the cost, complexity of integration, and insertion losses. Applications requiring true continuous tunability encourage exploration of new reconfiguration mechanisms for microwave resonators and filters.

Recently, a materials-based approach capable of continuous reconfiguration for microwave and RF devices has been studied [14-16]. This thesis proposes a fluidic-reconfigurable X-band SIW resonator capable of continuous tunability across the

reconfiguration range. Two inductive posts embedded in an SIW form a fixed resonator. A fluidic dielectric post between the inductive posts serves as the tuning mechanism. The volume fraction \mathcal{V} of high dielectric particles dispersed in low-loss oil defines material properties of the fluidic dielectric post. By changing \mathcal{V} the resonator characteristics can be manipulated. The variation of \mathcal{V} can be continuous, thus, the resonator can be continuously tuned.

Conceptual and advanced circuit modeling and field theory incorporating cavity material perturbations will be provided in the analysis of the tunable SIW resonator. Full-wave simulation will be used to verify analytical models and predict the physical resonator performance with estimated material properties of the fluidic dispersion. Measured data will be taken on the fabricated resonator using a network analyzer for a sampling of fluidic dispersion \mathcal{V} 's as proof of concept. A discrepancy between simulated and fabricated models leads to a second design iteration. The estimations used for the fluid/particle material properties are found to be inaccurate. New estimations, containing much higher loss are proposed by comparing simulated and measured data. A free-space and coaxial fixture material measurement system are fabricated in order to expand research efforts in finding low-loss microwave fluidic dispersions. A thorough analysis of the electromagnetic theory behind the data processing technique provides confidence in the measurements. Initial measurements on known permittivity samples reveal the accuracy of the measurement systems.

CHAPTER II
BACKGROUND

2.1 Network Analysis

In this work basic two-port network analysis techniques and concepts are applied to a microwave resonator. A two-port network and network variables are shown in Fig. 1. The analysis of the two-port network follows [2]. Voltmeters and ammeters for directly measuring the voltages and currents in Fig. 1 at microwave frequencies do not exist. Network analyzers measuring the reflected and transmitted waves across a microwave network are used instead. However, describing a network in terms of circuit components, voltages, and currents aid electrical engineers in the design process of microwave resonator, filters, and other such devices.

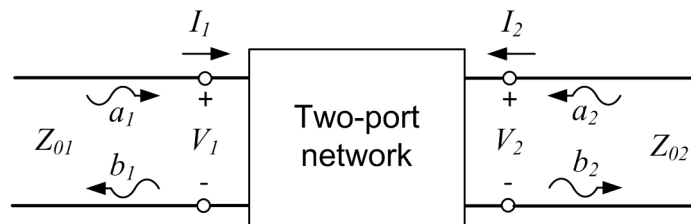


Fig. 1. Two-port network showing network variables.

The $ABCD$ parameters of a two-port network are very useful when analyzing cascaded complex two-port sub-networks and are defined as

$$\begin{aligned}
 A &= \left. \frac{V_1}{V_2} \right|_{I_2=0} & B &= \left. \frac{V_1}{-I_2} \right|_{V_2=0} \\
 C &= \left. \frac{I_1}{V_2} \right|_{I_2=0} & D &= \left. \frac{I_1}{-I_2} \right|_{V_2=0}
 \end{aligned} \tag{2.1}$$

The $ABCD$ parameters can be defined in a set of linear equation in matrix notation as

$$\begin{bmatrix} V_1 \\ I_1 \end{bmatrix} = \begin{bmatrix} A & B \\ C & D \end{bmatrix} \begin{bmatrix} V_2 \\ -I_2 \end{bmatrix}, \quad (2.2)$$

where the matrix of the $ABCD$ parameters is known as the $ABCD$ matrix of the network.

The negative sign in front of I_2 signifies opposite current direction in Fig. 1. The two-port networks used in this work and their $ABCD$ parameters are shown in Fig. 2.

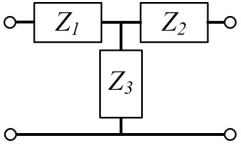
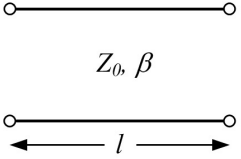
Circuit	$ABCD$ Parameters	
	$A = 1 + \frac{Z_1}{Z_3}$	$B = Z_1 + Z_2 + \frac{Z_1 Z_2}{Z_3}$
	$C = \frac{1}{Z_3}$	$D = 1 + \frac{Z_2}{Z_3}$
	$A = \cos \beta l$	$B = jZ_0 \sin \beta l$
	$C = jY_0 \sin \beta l$	$D = \cos \beta l$

Fig. 2. Useful two-port networks and their $ABCD$ parameters.

The S parameters of a two-port network relate the incident and reflected wave at the ports and are directly measurable by a network analyzer. The S parameters defined in terms of the wave variables of the two-port network in Fig. 1 are

$$\begin{aligned} S_{11} &= \left. \frac{b_1}{a_1} \right|_{a_2=0} & S_{12} &= \left. \frac{b_1}{a_2} \right|_{a_1=0} \\ S_{21} &= \left. \frac{b_2}{a_1} \right|_{a_2=0} & S_{22} &= \left. \frac{b_2}{a_2} \right|_{a_1=0} \end{aligned}, \quad (2.3)$$

where $a_n = 0$ implies a perfectly impedance match at port n . The S parameters of a two-port network can also be written as a set of linear equations in matrix notation as

$$\begin{bmatrix} b_1 \\ b_2 \end{bmatrix} = \begin{bmatrix} S_{11} & S_{12} \\ S_{21} & S_{22} \end{bmatrix} \begin{bmatrix} a_1 \\ a_2 \end{bmatrix}. \quad (2.4)$$

The general parameter S_{mn} is read as the S parameter from port “ n ” to port “ m ”. Thus, the S_{11} and S_{22} parameters are the reflection coefficients, whereas S_{12} and S_{21} are the transmission coefficients. The magnitude of the S parameters are often expressed in decibels (dB) defined as

$$|S_{mn}|_{dB} = 20 \log |S_{mn}|. \quad (2.5)$$

The limits and physical interpretations of S parameters are defined in Table 1.

Table 1. Limits and physical interpretations of two-port S parameters.

Parameter Value	S_{11}	S_{12}	S_{21}	S_{22}
0 ($-\infty$ dB)	Total transmission through port 1	Zero transmission from port 2 to 1	Zero transmission from port 1 to 2	Total transmission through port 2
1 (0 dB)	Total reflection at port 1	Total transmission from port 2 to 1	Total transmission from port 1 to 2	Total reflection at port 2

The $ABCD$ parameters analyze the circuit modeling of the resonator in this work and S parameters are physically measured from the fabricated device. Conversion between the two parameter types allows for comparison between the measured results and model. The network S parameters in terms of $ABCD$ parameters are

$$\begin{aligned}
S_{11} &= \frac{A + B/Z_0 - CZ_0 - D}{A + B/Z_0 + CZ_0 + D} & S_{21} &= \frac{2}{A + B/Z_0 + CZ_0 + D} \\
S_{12} &= \frac{2(AD - BC)}{A + B/Z_0 + CZ_0 + D} & S_{22} &= \frac{-A + B/Z_0 - CZ_0 + D}{A + B/Z_0 + CZ_0 + D}.
\end{aligned} \tag{2.6}$$

2.2 Substrate Integrated Waveguides

Rectangular waveguides (RWGs) are early forms of microwave transmissions lines still used in many applications today [2]. Fig. 3 shows the geometry of a RWG structure. The guide is assumed to be filled with a material of permittivity ϵ and permeability μ . The conductor walls of the waveguide from one solid piece of metal capable of supporting TE and TM mode propagation. TEM modes will not propagate due to the lack of a second conductor. By convention, $a > b$ such that the shortest side of the waveguide always resided along the y -axis.

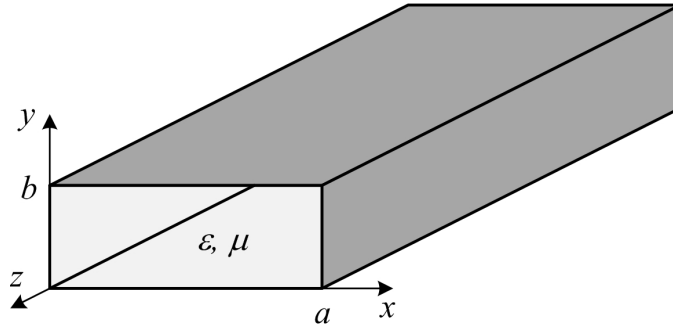


Fig. 3. Geometry of a conventional rectangular waveguide (RWG).

Substrate integrated waveguide (SIW) structures have recently provided a low-cost, low-profile alternative to conventional RWG by conforming the waveguide to planar form [3, 4]. Fig. 4 shows the geometry of an SIW structure. Rows of periodic vias

replace the lateral walls of the RWG in Fig. 3. The diameter of the vias d and center-to-center spacing s ensure very low leakage in the guide based on the criteria [17]

$$\begin{aligned} s/d &< 2.5 \\ d/W_{siw} &< 1/8. \end{aligned} \quad (2.7)$$

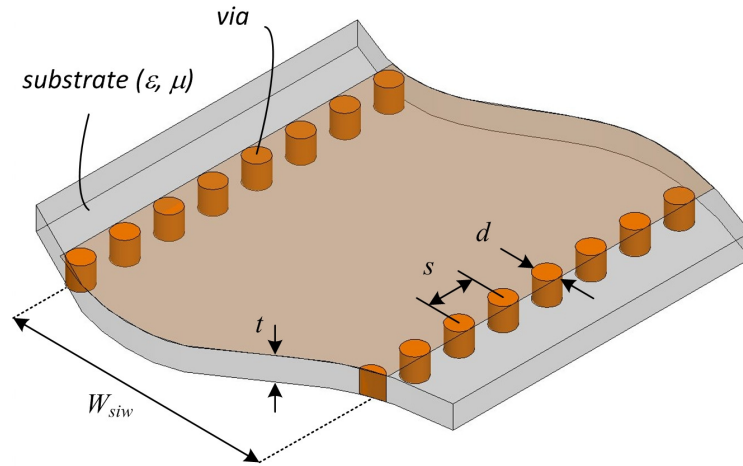


Fig. 4. Geometry of a substrate integrated waveguide (SIW).

With (2.7) satisfied, the SIW can be modeled by the RWG in Fig. 3 with $b = t$ and

$$a = a_{siw} = W_{siw} - 1.08 \frac{d^2}{s} + 0.1 \frac{d^2}{W_{siw}}, \quad (2.8)$$

due to the non-uniform fields along the rows of periodic vias [17]. The choice of substrate defines the (ϵ, μ) of the guide material. Neither TM_{mn} (for all m and n) nor TE_{mn} (with $n \neq 0$) modes propagate in an SIW due to large amounts of radiation between the vias caused by the discontinuous surface currents along the lateral walls [17]. Thus, the propagation constant of an SIW modeled as the RWG is

$$\beta = \sqrt{k^2 - k_c^2} = \sqrt{k^2 - \left(\frac{m\pi}{a_{siw}}\right)^2} = \sqrt{(2\pi f)^2 \mu\epsilon - \left(\frac{m\pi}{a_{siw}}\right)^2}. \quad (2.9)$$

The term k defines the wave number for TEM propagation in the substrate material. When $k > k_c$ the wave propagates in the SIW and attenuates when $k < k_c$. The cutoff frequency for the SIW TE_{m0} mode is

$$f_{c,m} = \frac{1}{2\pi\sqrt{\mu\epsilon}} \frac{m\pi}{a_{siw}}. \quad (2.10)$$

For a given mode, all frequencies lower than $f_{c,m}$ attenuate and all frequencies greater than $f_{c,m}$ propagate in the SIW. The lowest order (dominate) mode in the SIW is the TE_{10} mode with cutoff frequency

$$f_{c,1} = f_c = \frac{1}{2a_{siw}\sqrt{\mu\epsilon}}. \quad (2.11)$$

The guide wavelength in the SIW can then be compute by

$$\lambda_g = \frac{2\pi}{\beta}. \quad (2.12)$$

A 50Ω characteristic impedance often defines the input and output ports of a system or test equipment. Typically, the characteristic impedance of an SIW does not equal 50Ω and is smaller than the characteristic impedance of a conventional RWG (where $b = a/2$ in Fig. 3) due to the small t/a_{siw} for SIWs [18]. An approximation to the SIW characteristic impedance is

$$Z_{0,siw} = \frac{t}{a_{siw}} \frac{k\eta}{\beta}, \quad (2.13)$$

where $\eta = \sqrt{\mu/\varepsilon}$ for the substrate material. Common 50 Ω input/output ports for planar topology are microstrip lines. The width a microstrip line W for a desired characteristic impedance Z_0 on a substrate of thickness t and permittivity $\varepsilon = \varepsilon_0\varepsilon_r$ can be estimated from the first-order approximation [2]

$$\frac{W}{t} = \begin{cases} \frac{8e^A}{e^{2A} - 2} & \text{for } \frac{W}{t} < 1 \\ \frac{2}{\pi} \left[B - 1 - \ln(2B - 1) + \frac{\varepsilon_r - 1}{2\varepsilon_r} \left\{ \ln \left(B - 1 + 0.39 - \frac{0.61}{\varepsilon_r} \right) \right\} \right] & \text{for } \frac{W}{t} > 1 \end{cases} \quad (2.14)$$

where

$$A = \frac{Z_0}{60} \sqrt{\frac{\varepsilon_r + 1}{2}} + \frac{\varepsilon_r - 1}{\varepsilon_r + 1} \left(0.23 + \frac{0.11}{\varepsilon_r} \right)$$

$$B = \frac{377\pi}{2Z_0\sqrt{\varepsilon_r}}.$$

A tapered microstrip transmission line section (Fig. 5) can be used as a transition between a 50 Ω microstrip line and SIW [19]. The width of the 50 Ω microstrip line W_{50} and tapered microstrip section at the SIW opening W_{tap} can be estimated by substituting $Z_0 = 50$ and (2.13) into (2.14), respectively. The length of the tapered microstrip section L_{tap} should be long enough to provide a smooth transition between the quasi-TEM microstrip line mode to the TE₁₀ SIW mode and can be approximated by π/k . Once W_{50} , W_{tap} , and L_{tap} have been predicted, full-wave simulation refines these values for optimal performance.

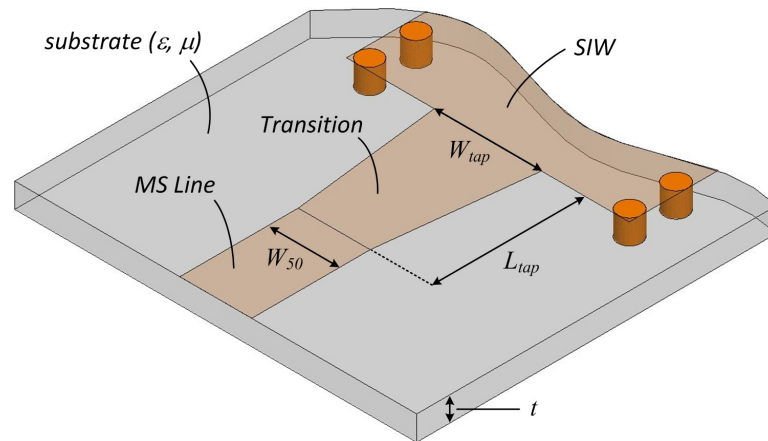


Fig. 5. Tapered transition between a $50\ \Omega$ microstrip line and SIW.

2.3 Microwave Resonators

Microwave resonators are key components of most filter designs [2]. The resonant frequency f_0 and quality factor Q describe the fundamental operation and performance of a resonator. Fig. 6 shows a conventional microwave resonator. The conductive walls of the rectangular cavity enclose a material with properties (ϵ, μ) .

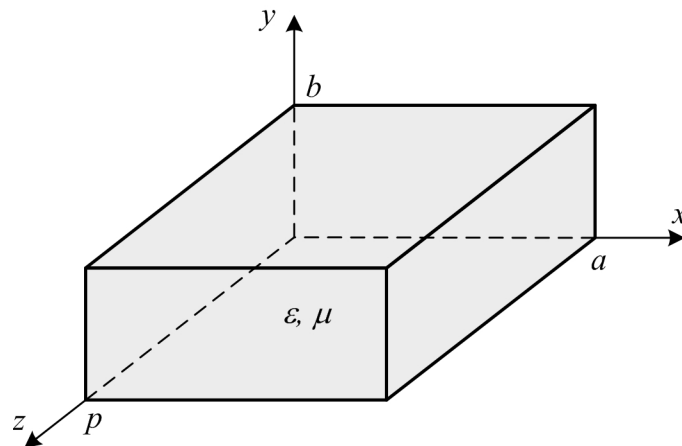


Fig. 6. Geometry of a conventional rectangular resonant cavity.

The analysis of the resonator follows [2]. The dimensions of the cavity and material properties determine the resonant frequency of the cavity,

$$f_{mnl} = \frac{1}{2\pi\sqrt{\mu\varepsilon}} \sqrt{\left(\frac{m\pi}{a}\right)^2 + \left(\frac{n\pi}{b}\right)^2 + \left(\frac{l\pi}{p}\right)^2}. \quad (2.15)$$

The indices m , n , and l are integers determining the number of half-wave variations along the x , y , and z directions, respectively. The dominate mode for the rectangular cavity is the TE₁₀₁ mode with resonate frequency,

$$f_0 = \frac{1}{2\sqrt{\mu\varepsilon}} \sqrt{\frac{1}{a^2} + \frac{1}{p^2}}. \quad (2.16)$$

The fields in the cavity for the TE₁₀₁ mode are,

$$E_x = E_0 \sin\left(\frac{\pi x}{a}\right) \sin\left(\frac{\pi z}{p}\right), \quad (2.17)$$

$$H_x = \frac{-jaE_0}{\eta\sqrt{a^2 + p^2}} \sin\left(\frac{\pi x}{a}\right) \cos\left(\frac{\pi z}{p}\right), \quad (2.18)$$

$$H_z = \frac{jpE_0}{\eta\sqrt{a^2 + p^2}} \cos\left(\frac{\pi x}{a}\right) \sin\left(\frac{\pi z}{p}\right). \quad (2.19)$$

The Q of the cavity resonator is a dimensionless parameter signifying loss defined as,

$$Q = \frac{\omega_0 \times \text{average energy stored}}{(\text{power loss})} = \omega_0 \frac{W_e + W_m}{P_l} \quad (2.20)$$

where W_e and W_m denote the stored electric and magnetic energies, respectively. A very low-loss resonator implies a very high Q . The stored electric energy is,

$$W_e = \frac{\varepsilon}{4} \int_V \mathbf{E} \cdot \mathbf{E}^* dv = \frac{\varepsilon}{4} \int_0^p \int_0^b \int_0^a |E_y|^2 dx dy dz = \frac{\varepsilon}{16} |E_0|^2 abp. \quad (2.21)$$

From the conservation of complex power $W_m = W_e$. The power lost from the conductive walls of the resonator is,

$$\begin{aligned}
 P_c &= \frac{R_s}{2} \int_{\substack{\text{cavity} \\ \text{walls}}} |\mathbf{H}|^2 ds \\
 &= \frac{R_s}{2} \left[2 \int_0^p \int_0^a \left(|H_x(y=0)|^2 + |H_z(y=0)|^2 \right) dx dz + 2 \int_0^b \int_0^a |H_x(z=0)|^2 dx dy \right. \\
 &\quad \left. + 2 \int_0^p \int_0^b |H_z(x=0)|^2 dy dz \right] \\
 &= \frac{|E_0|^2 R_s}{4\eta^2 (a^2 + p^2)} \left[ap(a^2 + p^2) + 2b(a^3 + p^3) \right]. \tag{2.22}
 \end{aligned}$$

The surface resistivity is defined as $R_s = \sqrt{\omega\mu_0/2\sigma}$ where μ_0 and σ denote the permeability of free-space and the conductivity of the conductive walls, respectively.

The quality factor from the conductive losses in the cavity is then,

$$Q_c = \frac{2\omega W_e}{P_c} = \frac{\pi\eta}{2R_s} \frac{b(a^2 + p^2)^{3/2}}{ap(a^2 + p^2) + 2b(a^3 + p^3)}. \tag{2.23}$$

If losses are present in the dielectric material of the cavity such that $\varepsilon = \varepsilon' - j\varepsilon'' = \varepsilon'(1 - \varepsilon''/\varepsilon') = \varepsilon'(1 - \tan \delta)$ then the power lost due to the dielectric is,

$$P_d = \frac{\omega\varepsilon''}{2} \int_V |\mathbf{E}|^2 dv = \frac{\omega\varepsilon''}{2} \int_0^p \int_0^b \int_0^a |E_y|^2 dx dy dz = \frac{\omega\varepsilon'' |E_0|^2 abp}{8}. \tag{2.24}$$

The quality factor from the dielectric becomes,

$$Q_d = \frac{2\omega W_e}{P_d} = \frac{1}{\tan \delta}. \tag{2.25}$$

The quality factor when both conductive and dielectric losses are present is,

$$\frac{1}{Q} = \frac{1}{Q_c} + \frac{1}{Q_d}. \quad (2.26)$$

2.4 Cavity Material Perturbations

Consider the general cavity material perturbation scenario depicted in Fig. 7. Let \mathbf{E}_0 , \mathbf{H}_0 , and ω_0 represent the vector fields and resonant frequency in the original cavity of material properties (ϵ, μ) . When perturbation of the cavity by $(\Delta\epsilon, \Delta\mu)$ occurs, the vector fields and resonant frequency become \mathbf{E} , \mathbf{H} , and ω , respectively. By manipulating the field equations of the original and perturbed cavities it can be shown that the change in resonant frequency of the perturbed cavity is [20],

$$\frac{\omega - \omega_0}{\omega} = -\frac{\int_V (\Delta\epsilon \mathbf{E} \cdot \mathbf{E}_0^* + \Delta\mu \mathbf{H} \cdot \mathbf{H}_0^*) dv}{\int_V (\epsilon \mathbf{E} \cdot \mathbf{E}_0^* + \mu \mathbf{H} \cdot \mathbf{H}_0^*) dv}, \quad (2.27)$$

where V is the volume of the cavity enclosed by S . The formulation of (2.27) assumes ϵ , μ , $\Delta\epsilon$, and $\Delta\mu$ are real.

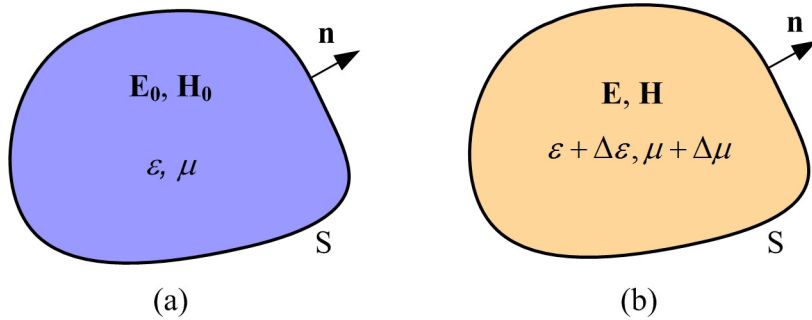


Fig. 7. Cavity material perturbation theory (a) original cavity and (b) perturbed cavity.

2.5 Maxwell-Garnett Mixing Rule

The Maxwell-Garnett (MG) mixing rule models the effective dielectric property of a fluidic dispersion [21]. Consider a fluidic medium (ϵ_1) in which inclusion particles (ϵ_2) of an arbitrary shape have been dispersed. The combined volumes of medium and particles create the dispersion (ϵ_{eff}). The ratio of the volume of particles to volume of the fluidic dispersion denotes the volume fraction of the inclusion particles \mathcal{V} . Along with \mathcal{V} , the geometry of the inclusion particles characterize ϵ_{eff} . Fig. 8 plots the MG mixing rule for a fluidic dispersion with spherical, needle, and disc shaped particle geometries.

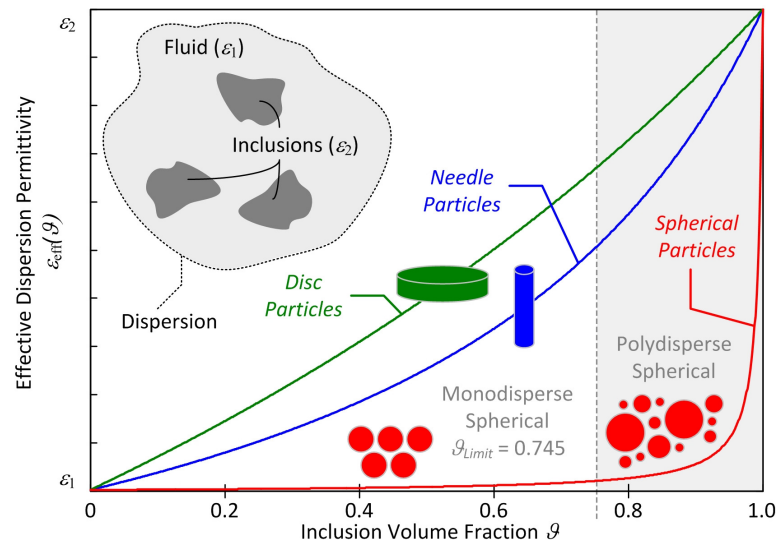


Fig. 8. Maxwell-Garnett mixing rule for fluidic dispersions utilizing spherical (red), needle (blue), and disc (green) particles.

The permittivity of the fluidic medium dominates the dispersion permittivity for spherical inclusion particles until very high \mathcal{V} 's are achieved utilizing polydispersity, multiple sized spherical particles. High aspect-ratio inclusion particles, such as, needle

or disc geometries, create a more linear relationship between \mathcal{G} and ε_{eff} . The exact definition of the spherical inclusion particle MG mixing rule plotted in Fig. 8 is

$$\varepsilon_{eff}(\mathcal{G}) = \varepsilon_1 + 3\mathcal{G}\varepsilon_1 \frac{\varepsilon_2 - \varepsilon_1}{\varepsilon_2 + 2\varepsilon_1 - \mathcal{G}(\varepsilon_2 - \varepsilon_1)}, \quad (2.28)$$

where ε_1 , ε_2 , and ε_{eff} can be complex to account for lossy materials. Similar MG mixing rule definitions for needle and disc particle geometries were used in Fig. 8.

2.6 Coupled Resonator Filters

Although this work focuses on the design and analysis of an SIW resonator, basic principles of coupled-resonator filters are summarized (from [1]) to demonstrate the resonator's potential in filter design. Fig. 9 depicts an n -pole coupled-resonator circuit for the narrowband bandpass filter Chebyshev response in Fig. 10. An inductor L in parallel with a capacitor C models each resonator with resonant frequency f_0 . The quality factor of each resonator delineates the insertion loss IL of the filter. The coefficients $k_{i,i+1}$ define the coupling between each resonator and k_{01} and $k_{n,n+1}$ define the external coupling from the source to first resonator and load to last resonator, respectively.

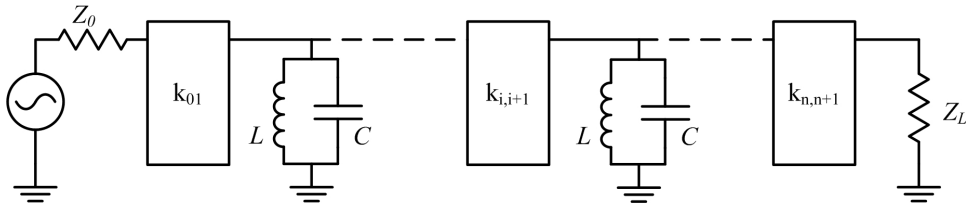


Fig. 9. n -pole coupled-resonator filter circuit.

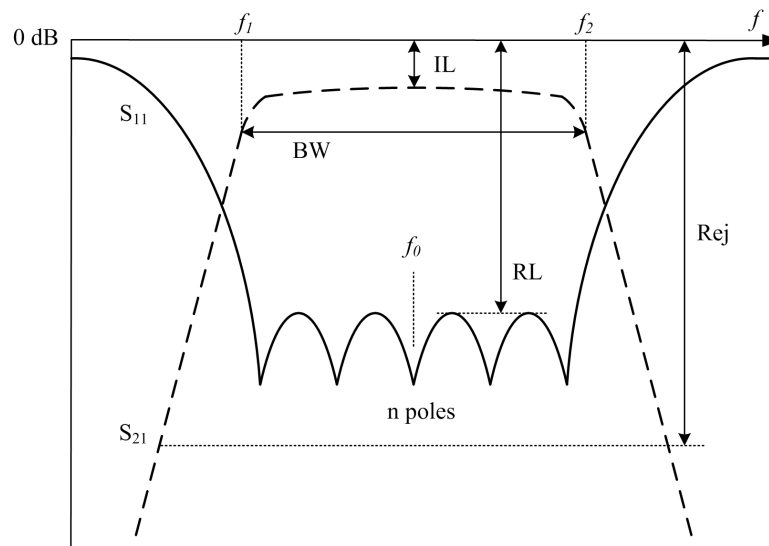


Fig. 10. Narrowband bandpass filter Chebyshev response.

The lowpass filter prototype values and fractional bandwidth $FBW = BW/f_0 = (f_2 - f_1)/f_0$ determine the coupling coefficient values. The desired return loss (RL) and out-of-band rejection (Rej) govern the necessary lowpass filter prototype values and order n of the filter. Tunable resonators implemented in Fig. 9 would allow f_0 to vary enabling manipulation of the passband characteristics in Fig. 10 for frequency selective applications.

CHAPTER III

ANALYSIS

3.1 The Static SIW Resonator

Two inductive posts embedded within an SIW structure form a static SIW resonator shown in Fig. 11. The diameter of the inductive post d matches the diameter of the SIW lateral wall vias for ease of fabrication. A very crude yet easily conceptual circuit model in Fig. 12 describes the resonator.

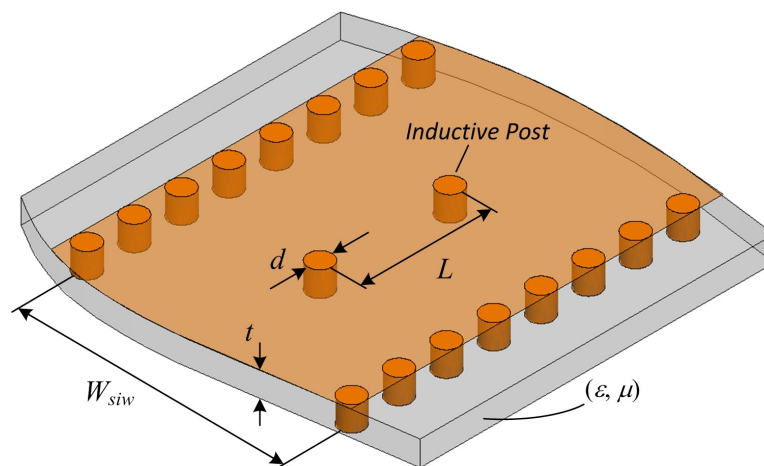


Fig. 11. The static SIW resonator.

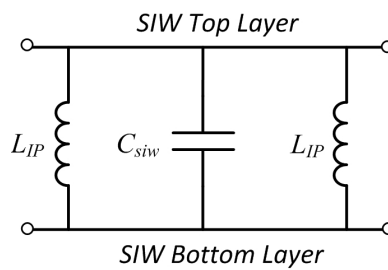


Fig. 12. Conceptual circuit model for the static SIW resonator.

The inductive posts are modeled by inductors L_{IP} because they allow current to transfer between the top and bottom layer of the SIW. The capacitor C_{siw} models the fields of the SIW section of length L between the two inductive posts. This forms a parallel resonant circuit which resonates when the stored electric energy from C_{siw} equals the stored magnetic energy from $L_{IP} \parallel L_{IP}$ at the frequency [2],

$$\omega_0 = \sqrt{\frac{2}{L_{IP} C_{siw}}}. \quad (3.1)$$

The fields of the SIW section between the inductive posts are not constant making C_{siw} very difficult to determine analytically, however the model in Fig. 12 clearly proves the structure in Fig. 11 operates as a resonator. Fig. 13 shows an advanced circuit model created from the T-network of an inductive post embedded in a RWG [22].

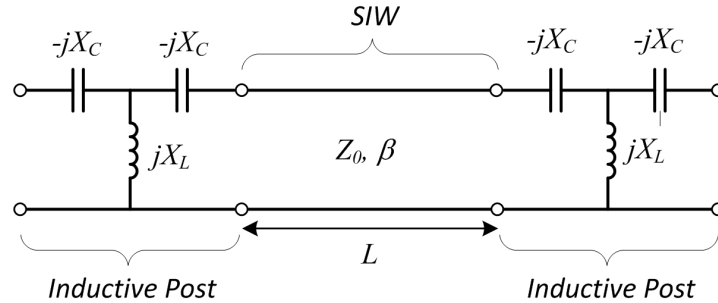


Fig. 13. Advanced circuit model for the static SIW resonator.

The Z_0 and β of the SIW transmission line section are determined from (2.13) and (2.9), respectively. The circuit parameters of the inductive post embedded in an SIW are [22]

$$\frac{X_L}{Z_0} - \frac{X_C}{2Z_0} = \frac{a_{siw}}{2\lambda_g} \left[S_0 - \left(\frac{\pi d}{2\lambda} \right)^2 - \frac{5}{8} \left(\frac{\pi d}{2\lambda} \right)^4 - 2 \left(\frac{\pi d}{2\lambda} \right)^4 \left(S_2 - 2S_0 \frac{\lambda^2}{\lambda_g^2} \right)^2 \right] \quad (3.2)$$

$$\frac{X_C}{Z_0} = \frac{a_{siw}}{\lambda_g} \frac{\left(\frac{\pi d}{a_{siw}} \right)^2}{1 + \frac{1}{2} \left(\frac{\pi d}{\lambda} \right) \left(S_2 + \frac{3}{4} \right)} \quad (3.3)$$

where

$$S_0 = \ln \left(\frac{4a_{siw}}{\pi d} \right) - 2 + 2 \sum_{n=3,5,\dots}^{\infty} \left[\left(n^2 - \left(\frac{2a_{siw}}{\lambda} \right)^2 \right)^{-\frac{1}{2}} - \frac{1}{n} \right],$$

$$S_2 = \ln \left(\frac{4a_{siw}}{\pi d} \right) - \frac{5}{2} + \frac{11}{3} \left(\frac{\lambda}{2a_{siw}} \right)^2 - \left(\frac{\lambda}{a_{siw}} \right)^2 \sum_{n=3,5,\dots}^{\infty} \left[\sqrt{n^2 - \left(\frac{2a_{siw}}{\lambda} \right)^2} - n + \frac{2}{n} \left(\frac{a_{siw}}{\lambda} \right)^2 \right].$$

The wavelength $\lambda = \frac{2\pi}{k} = \frac{1}{\sqrt{\mu\epsilon}f}$ denotes the wavelength in the substrate material. The

individual $ABCD$ parameters of the inductive post ($A_{IP}, B_{IP}, C_{IP}, D_{IP}$) and SIW ($A_{siw}, B_{siw}, C_{siw}, D_{siw}$) can be found using the relations in Fig. 2. The cascaded individual networks form the complete $ABCD$ matrix of the static SIW resonator given by (3.4). The $ABCD$ parameters can be converted to S parameter using (2.6) to find the complete frequency response of the static SIW resonator.

$$\begin{bmatrix} A_{sr} & B_{sr} \\ C_{sr} & D_{sr} \end{bmatrix} = \begin{bmatrix} A_{IP} & B_{IP} \\ C_{IP} & D_{IP} \end{bmatrix} \begin{bmatrix} A_{siw} & B_{siw} \\ C_{siw} & D_{siw} \end{bmatrix} \begin{bmatrix} A_{IP} & B_{IP} \\ C_{IP} & D_{IP} \end{bmatrix} \quad (3.4)$$

The circuit model analysis supports an intuitive understanding of the static SIW resonator and ability to compute the frequency response. However, the complexities of the advanced circuit model in Fig. 13 hinder the development of an analytical solution

for the resonant frequency f_0 and unloaded quality factor Q_u , the Q when not loaded by the SIW structure. An equivalent cavity model for the static resonator (Fig. 14) enables the possibility to solve for f_0 and Q_u . The edges of the equivalent cavity in the SIW are depicted in blue dashed lines.

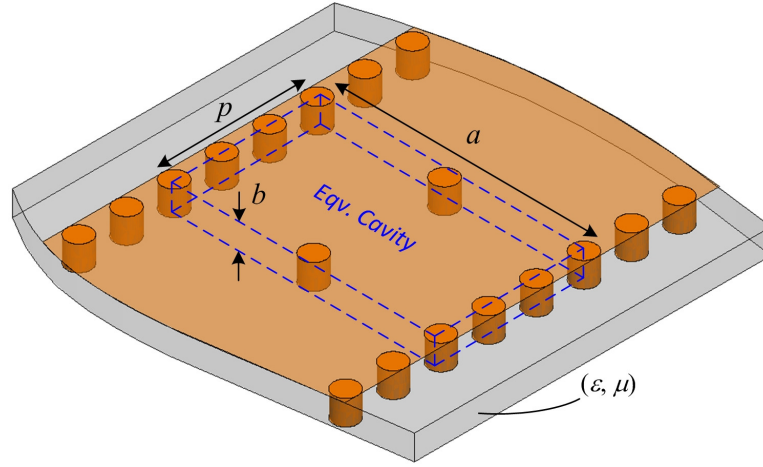


Fig. 14. Equivalent cavity for the static SIW resonator.

The cavity can be directly analyzed as the rectangular cavity in Fig. 6 with $a = a_{siw}$, $b = t$, and $p = L + d$. From (2.16) and (2.26),

$$f_0 = \frac{1}{2\sqrt{\mu\epsilon}} \sqrt{\frac{1}{a_{siw}^2} + \frac{1}{(L+d)^2}}, \quad (3.5)$$

$$\frac{1}{Q_u} = \frac{1}{\tan \delta} + \frac{2R_s}{\pi\eta} \frac{a_{siw}^3 (L+d+2t) + (L+d)^3 (a_{siw}+2t)}{t(a_{siw}^2 + L^2 + d^2 + 2dL)^{3/2}}. \quad (3.6)$$

The dimension p extends to the outer edge of the inductive post to account for the field extensions from energy coupling around the inductive posts.

3.2 Reconfiguration Mechanism

In this work, a dielectric post of variable material properties (Fig. 15) centered in the static SIW resonator facilitates resonant frequency reconfiguration. A fluidic dispersion of high dielectric particles ε_2 in a low-loss low dielectric fluid ε_1 at a volume fraction \mathcal{G} constructs the dielectric post. The MG mixing rule estimates the fluidic dispersion's effective dielectric property $\varepsilon_d(\mathcal{G}) = \varepsilon_{eff}(\mathcal{G})$ for spherical particles using (2.28). In this work the permeability of the dielectric post $\mu_d = \mu_0$. Fig. 16 shows the conceptual dynamics of adding the variable permittivity dielectric post.

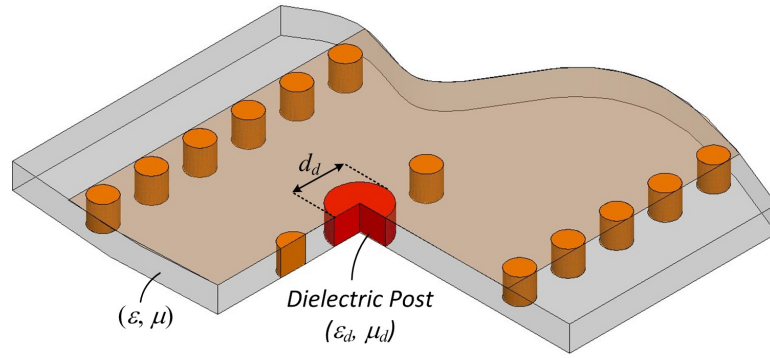


Fig. 15. The tunable SIW resonator with the fluidic dispersion (red).

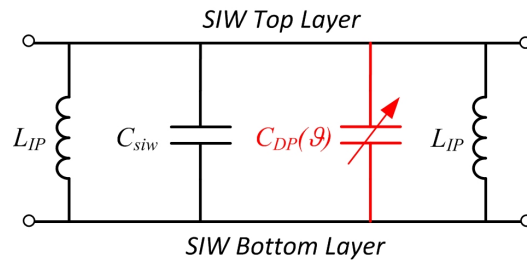


Fig. 16. Conceptual circuit model for the tunable SIW resonator.

The variable dielectric post in the resonator can be model as an additional variable capacitor $C_{DP}(\mathcal{G})$. The resonant frequency becomes a function of \mathcal{G} given by

$$\omega_0(\mathcal{G}) = \sqrt{\frac{2(C_{DP}(\mathcal{G}) + C_{siw})}{L_{IP}C_{siw}C_{DP}(\mathcal{G})}}. \quad (3.7)$$

The difficulty in computing C_{siw} makes (3.7) challenging to solve; however, the conceptual model unveils the reconfiguration potential by controlling \mathcal{G} in the fluidic dispersion. Fig. 17 illustrates an advanced circuit model created from the T-network of a dielectric post in a RWG [22].

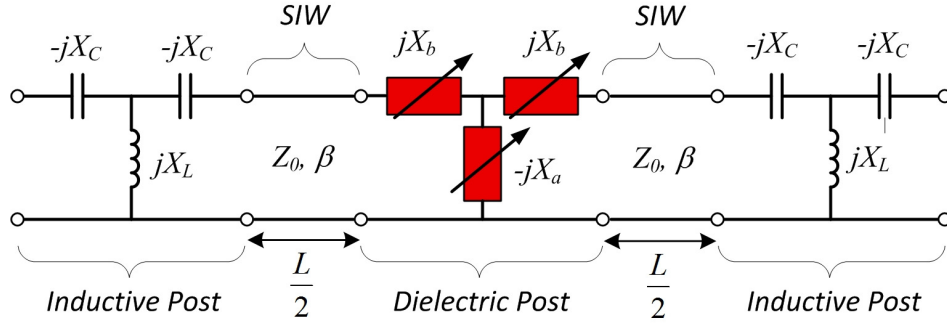


Fig. 17. Advanced circuit model for the tunable SIW resonator.

The circuit parameters of the dielectric post for real ϵ_d are [22]

$$\frac{X_a(\mathcal{G})}{Z_0} - \frac{X_b(\mathcal{G})}{Z_0} = \frac{a_{siw}}{2\lambda_g} \left[\frac{2\lambda^2}{(\epsilon_n(\mathcal{G}) - 1)(\pi d)^2} - S_0 - \frac{1}{4} \frac{\epsilon_n(\mathcal{G}) - 3}{\epsilon_n(\mathcal{G}) - 1} \right] \quad (3.8)$$

$$\frac{X_b(\mathcal{G})}{Z_0} = \frac{a_{siw}}{8\lambda_g} \left(\frac{a_{siw}}{\lambda} \right)^2 (\epsilon_n(\mathcal{G}) - 1) \left(\frac{\pi d}{a_{siw}} \right)^4 \left(1 + \frac{\epsilon_n(\mathcal{G}) - 2}{6} \left(\frac{\pi d}{\lambda} \right)^2 \right), \quad (3.9)$$

where

$$\varepsilon_n(\mathcal{G}) = \frac{\varepsilon_d(\mathcal{G})}{\varepsilon} = \frac{\varepsilon_{rd}(\mathcal{G})\varepsilon_0}{\varepsilon_r\varepsilon_0} = \frac{\varepsilon_{rd}(\mathcal{G})}{\varepsilon_r},$$

and S_0 is given in (3.2) and (3.3). When the fluidic dispersion contains losses, such that $\varepsilon_d(\mathcal{G}) = \varepsilon'_d(\mathcal{G}) - j\varepsilon''_d(\mathcal{G})$ the formulas in (3.8) and (3.9) are still valid provided $X_a(\mathcal{G})/Z_0$ and $X_b(\mathcal{G})/Z_0$ are replaced with $j(Z_a(\mathcal{G})/Z_0)$ and $-j(Z_b(\mathcal{G})/Z_0)$, respectively. The $ABCD$ parameters of the dielectric post ($A_{DP}(\mathcal{G})$, $B_{DP}(\mathcal{G})$, $C_{DP}(\mathcal{G})$, $D_{DP}(\mathcal{G})$) and half the SIW section (A_{hsw} , B_{hsw} , C_{hsw} , D_{hsw}) can be found using the relations in Fig. 2. The complete $ABCD$ matrix for the tunable SIW resonator is given by (3.10). The $ABCD$ parameters can be converted to S parameter using (2.6) to find the complete frequency response of the tunable SIW resonator.

$$\begin{bmatrix} A_{tr}(\mathcal{G}) & B_{tr}(\mathcal{G}) \\ C_{tr}(\mathcal{G}) & D_{tr}(\mathcal{G}) \end{bmatrix} = \begin{bmatrix} A_{IP} & B_{IP} \\ C_{IP} & D_{IP} \end{bmatrix} \begin{bmatrix} A_{hsw} & B_{hsw} \\ C_{hsw} & D_{hsw} \end{bmatrix} \begin{bmatrix} A_{DP}(\mathcal{G}) & B_{DP}(\mathcal{G}) \\ C_{DP}(\mathcal{G}) & D_{DP}(\mathcal{G}) \end{bmatrix}. \quad (3.10)$$

$$\begin{bmatrix} A_{hsw} & B_{hsw} \\ C_{hsw} & D_{hsw} \end{bmatrix} \begin{bmatrix} A_{IP} & B_{IP} \\ C_{IP} & D_{IP} \end{bmatrix}$$

As with the static resonator, the complexities of the tunable resonator's advanced circuit model hinder the development of closed-form solutions for $f_0(\mathcal{G})$ and $Q_u(\mathcal{G})$. The equivalent cavity model (Fig. 13) along with material perturbation theory (Section 2.4) provide the necessary tools for such formulations. Consider the equivalent cavity of the SIW resonator with a cylindrical volume of fluidic dispersion (dielectric post) placed in the center (Fig. 18). The fluidic dispersion can be viewed as a material perturbation of the original cavity.

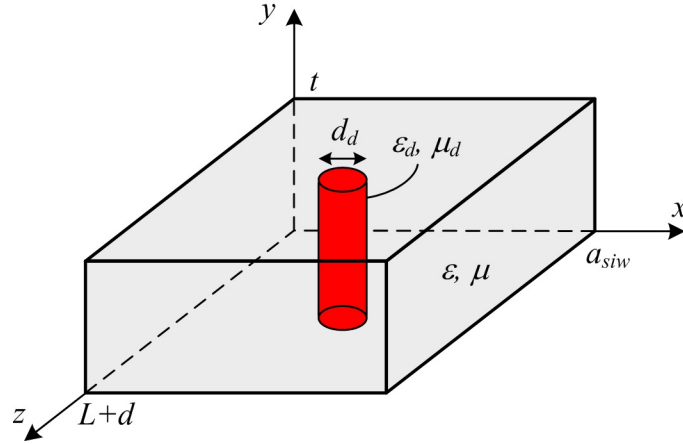


Fig. 18. Cavity material perturbation model for the tunable SIW resonator.

Eqn. (2.27) governs the shift in resonant frequency caused by the perturbation. The angular frequencies ω_0 and ω signify the resonant frequencies of the unperturbed and perturbed cavities, respectively. The change in permittivity $\Delta\varepsilon = \varepsilon_d - \varepsilon$ exists only within the volume of the fluidic dispersion. The permittivity ε_d and ε are assumed real. The notation ε_d and $\varepsilon_d(\mathcal{V})$ are interchangeable for the remainder of this thesis. In this work the change in permeability $\Delta\mu = 0$. Thus, (2.27) can be rewritten as

$$\frac{\omega - \omega_0}{\omega} = - \frac{\iiint_{\text{dispersion}} \Delta\varepsilon \mathbf{E} \cdot \mathbf{E}_0^* dv}{\iiint_{\text{cavity}} (\varepsilon \mathbf{E} \cdot \mathbf{E}_0^* + \mu \mathbf{H} \cdot \mathbf{H}_0^*) dv}. \quad (3.11)$$

The unperturbed vector fields of the original cavity \mathbf{E}_0 and \mathbf{H}_0 are defined in (2.17) - (2.19) where $a = a_{siw}$ and $p = L + d$. However, the perturbed vector fields \mathbf{E} and \mathbf{H} are unknown. For small dispersion volumes the perturbed vector fields across the volume of the cavity will not vary significantly. Thus, the approximations $\mathbf{E} = \mathbf{E}_0$ and $\mathbf{H} = \mathbf{H}_0$ in the denominator of (3.11) are valid. Consequently, the ω term in the denominator on the

right hand side (RHS) of (3.11) becomes ω_0 since only original fields are integrated in the denominator on the left hand side (LHS). Then (3.11) becomes

$$\frac{\omega - \omega_0}{\omega_0} = - \frac{\iiint_{dispersion} \Delta \varepsilon \mathbf{E} \cdot \mathbf{E}_0^* dv}{\iiint_{cavity} (\varepsilon \mathbf{E}_0 \cdot \mathbf{E}_0^* + \mu \mathbf{H}_0 \cdot \mathbf{H}_0^*) dv}. \quad (3.12)$$

The two integration terms in the denominator are recognized as proportions to the stored electric and magnetic energies of the unperturbed cavity which are equal from conservation of complex power [2]. Thus,

$$\frac{\omega - \omega_0}{\omega_0} = - \frac{\iiint_{dispersion} \Delta \varepsilon \mathbf{E} \cdot \mathbf{E}_0^* dv}{2 \iiint_{cavity} \varepsilon |\mathbf{E}_0|^2 dv}. \quad (3.13)$$

A quasi-static approximation to \mathbf{E} in the numerator for a cylindrical perturbation aligned with the electric field is $\mathbf{E} = \mathbf{E}_0$ [20]. Therefore,

$$\begin{aligned} \frac{\omega - \omega_0}{\omega_0} &= - \frac{\iiint_{dispersion} \Delta \varepsilon |\mathbf{E}_0|^2 dv}{2 \iiint_{cavity} \varepsilon |\mathbf{E}_0|^2 dv} \\ &= - \frac{\int_A \int_0^b (\varepsilon_d - \varepsilon) E_0^2 \sin^2 \left(\frac{\pi x}{a_{siv}} \right) \sin^2 \left(\frac{\pi z}{L+d} \right) dy dx dz}{2 \int_0^{L+d} \int_0^{a_{siv}} \int_0^b \varepsilon E_0^2 \sin^2 \left(\frac{\pi x}{a_{siv}} \right) \sin^2 \left(\frac{\pi z}{L+d} \right) dx dy dz} \\ &= - \frac{2(\varepsilon_d - \varepsilon)}{\varepsilon a_{siv} (L+d)} \int_A \int \sin^2 \left(\frac{\pi x}{a_{siv}} \right) \sin^2 \left(\frac{\pi z}{L+d} \right) dx dz, \end{aligned} \quad (3.14)$$

where A signifies the cross-section of the perturbation along the xz plane. The integrand of (3.14) can be approximated as unity for a thin centered post. The final closed-form solution becomes,

$$\frac{\omega(\mathcal{G}) - \omega_0}{\omega_0} = \frac{2(\varepsilon - \varepsilon_d(\mathcal{G}))}{\varepsilon a_{siv}(L+d)} A. \quad (3.15)$$

When a lossy fluidic dispersion perturbs the cavity such that $\varepsilon_d = \varepsilon'_d - j\varepsilon''_d$, the angular frequencies in (3.15) must be replaced with a complex effective resonant frequency [2] given by,

$$\omega \leftarrow \omega \left(1 + \frac{j}{2Q} \right), \quad (3.16)$$

where Q signifies the quality factor of the resonator. Substituting (3.16) into (3.15) for both ω and ω_0 yields

$$\frac{\omega \left(1 + \frac{j}{2Q} \right) - \omega_0 \left(1 + \frac{j}{2Q_0} \right)}{\omega_0 \left(1 + \frac{j}{2Q_0} \right)} = \frac{2(\varepsilon - \varepsilon'_d + j\varepsilon''_d)}{\varepsilon a_{siv}(L+d)} A, \quad (3.17)$$

where Q_0 and Q represents the *unloaded* quality factors of the unperturbed and perturbed resonator, respectively. The left hand side of (3.17) can be rearranged to

$$\frac{\omega \omega_0 \left(1 + \frac{1}{4QQ_0} \right) - \omega_0^2 \left(1 + \frac{1}{4Q_0^2} \right)}{\omega_0^2 \left(1 + \frac{1}{4Q_0^2} \right)} + j \frac{\omega \omega_0 \left(\frac{1}{2Q} - \frac{1}{2Q_0} \right)}{\omega_0^2 \left(1 + \frac{1}{4Q_0^2} \right)}. \quad (3.18)$$

Because $1 \gg \frac{1}{Q_0}$, (3.17) becomes

$$\frac{\omega - \omega_0}{\omega_0} + \frac{j}{2} \frac{\omega}{\omega_0} \left(\frac{1}{Q} - \frac{1}{Q_0} \right) = \frac{2(\varepsilon - \varepsilon'_d + j\varepsilon''_d)}{\varepsilon a_{siv}(L+d)} A. \quad (3.19)$$

Equating the real and imaginary parts of (3.19) and solving the set of equations renders the relationship,

$$\left(\frac{1}{Q(\mathcal{G})} - \frac{1}{Q_0} \right) = 2 \left(\frac{\varepsilon_d''(\mathcal{G})}{\varepsilon_d'(\mathcal{G}) - \varepsilon} \right) \left(\frac{\omega_0 - \omega(\mathcal{G})}{\omega(\mathcal{G})} \right). \quad (3.20)$$

The material properties of the dispersion and shift in resonance caused by the dispersion contribute to the Q . Small ε_d'' (low-loss fluidic dispersion) achieve a high Q throughout reconfiguration whereas, large ε_d'' (high-loss fluidic dispersion) decrease the Q .

CHAPTER IV

DESIGN ITERATION 1

4.1 Initial Dispersions

Silicone fluid (SF) (polydimethylsiloxane), $\epsilon_1/\epsilon_0 = (\epsilon_1' - j\epsilon_1'')/\epsilon_0 = \epsilon_{r1}(1 - j \tan \delta_1) \sim 2.8(1 - j0.001)$, and Barium Strontium Titanate (BSTO) ($\text{Ba}_{0.5}\text{Sr}_{0.5}\text{TiO}_3$), $\epsilon_2/\epsilon_0 = (\epsilon_2' - j\epsilon_2'')/\epsilon_0 = \epsilon_{r2}(1 - j \tan \delta_2) \sim 500(1 - j0.05)$, powder compose the initial fluidic dispersions. The spherical polydispersed BSTO particles have diameters < 100 nm. The SF is readily available over a wide range of viscosities. Higher viscosity SF stabilizes the mixed fluidic dispersion for an extend time period (hours). Lower viscosities facilitate the mixture of high φ fluidic dispersions. Fig. 19 shows the BSTO container and SEM image of the BSTO.

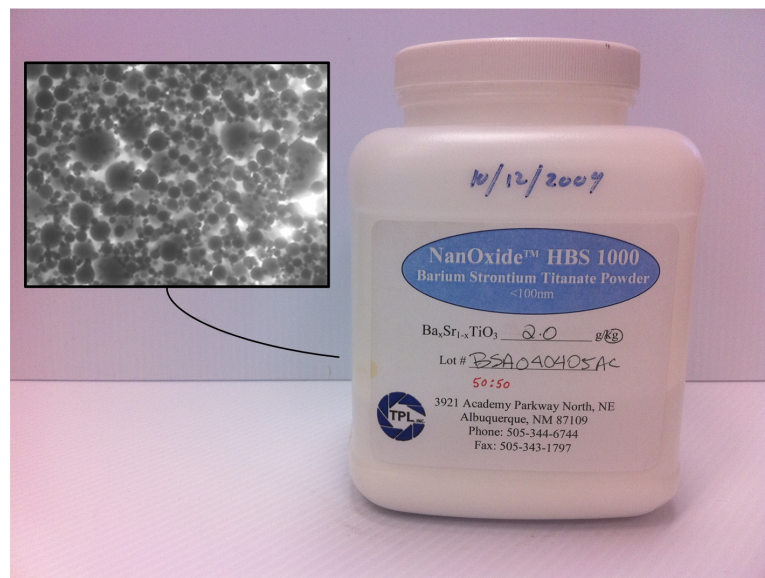


Fig. 19. BSTO used for initial dispersions with an SEM image.

A sampling of $\vartheta = 0, 0.25, 0.4,$ and 0.5 were mixed using 95-105, 350-550, and 950-1050 *cst* SF for the $\vartheta = 0.5, 0.4,$ and $0.25,$ respectively. The MG mixing rule predicts the fluidic dispersions effective material properties summarized in Table 2 with the same material property ε_1 used for all SF viscosities.

Table 2. Estimated ε_d for initial fluidic dispersions using the MG mixing rule

ϑ	$\varepsilon_d/\varepsilon_0 = \varepsilon_{rd}(1-j\tan\delta_d)$
0	$2.8(1-j0.001)$
0.25	$5.54(1-j0.0015)$
0.4	$8.25(1-j0.0019)$
0.5	$10.93(1-j0.0022)$

Although the fluidic dispersions for spherical particles are dominated by ε_1 over $0 < \vartheta < 0.5$, the large difference in ε'_2 and ε'_1 allows wide variance in ε'_d . The loss of the fluidic dispersion $\tan\delta_d$ remains low because the low-loss assumed for the SF.

4.2 Predicted Performance

The complete full-wave simulation model completed in Ansoft HFSS [23] for the tunable SIW resonator is shown in Fig. 20 (dimensions in Table 3). Not shown in Fig. 20 is the completely metalized ground plane. The substrate is Duriod 5870 ($\varepsilon/\varepsilon_0 = 2.33$) and the vias are composed of copper. Small openings on the top and bottom of the dielectric post allowing fluid flow are assumed negligible and not modeled. The values of W_{50} , W_{tap} , and L_{tap} provide $S_{11} < -10$ dB across X-band for the SIW structure. The MG

mixing rule was built into HFSS such that ε_d could be easily varied according to ϑ . The frequency response predicted from HFSS compared to the response predicted from the circuit model for the fluidic-reconfigurable resonator is shown in Fig. 21 and Fig. 22.

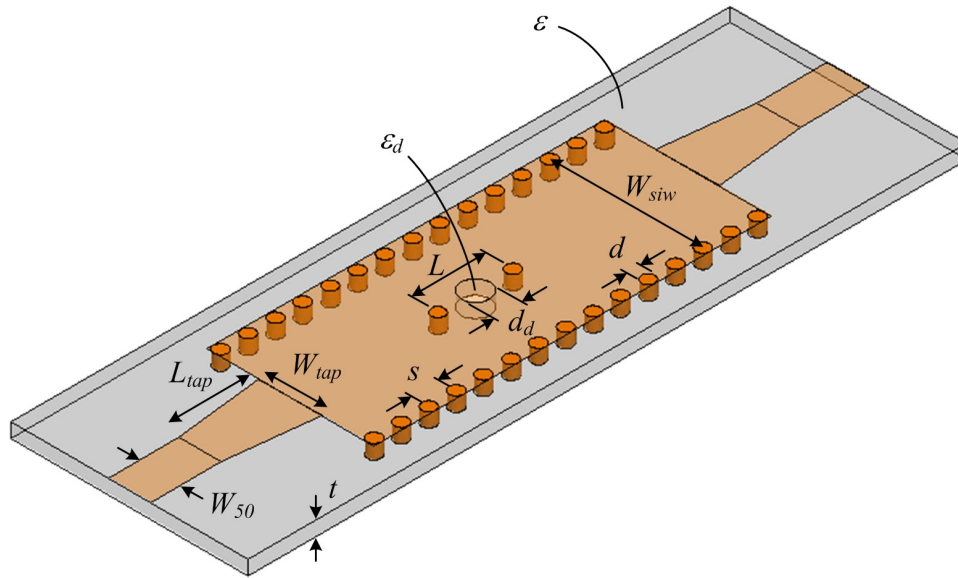


Fig. 20. Complete HFSS simulation model for the initial tunable SIW resonator.

Table 3. Dimensions of the initial tunable SIW resonator

Parameter	Dimension (mm)
d	1.5113
d_d	3.175
L	8.3
L_{tap}	10
s	3.0226
t	1.5748
W_{50}	4.7
W_{siw}	16.9113
W_{tap}	7

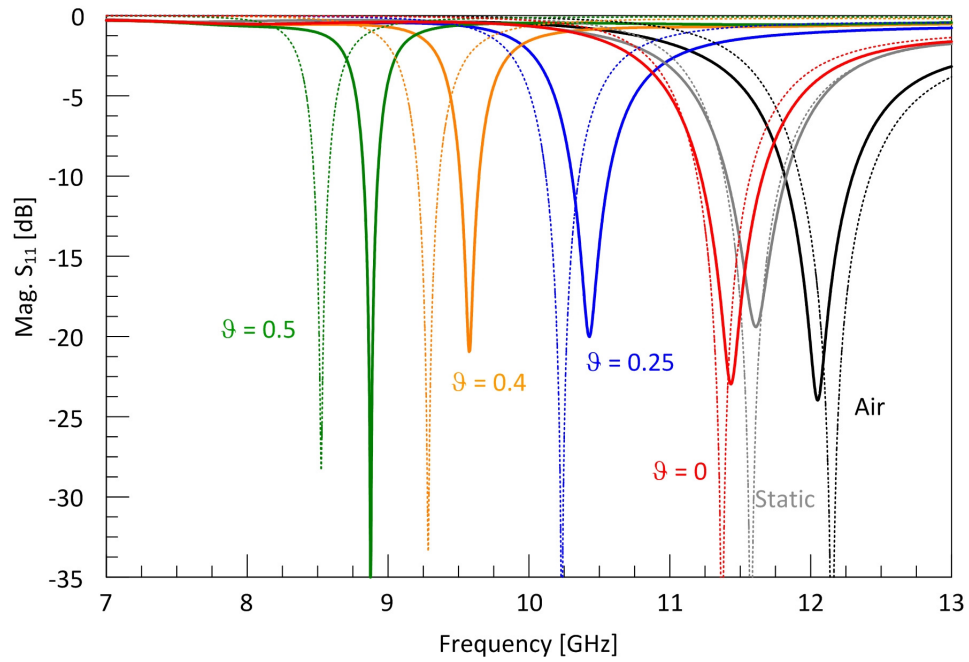


Fig. 21. Circuit model (dotted) and HFSS simulation (solid) predicted S_{11} response for the initial tunable SIW resonator.

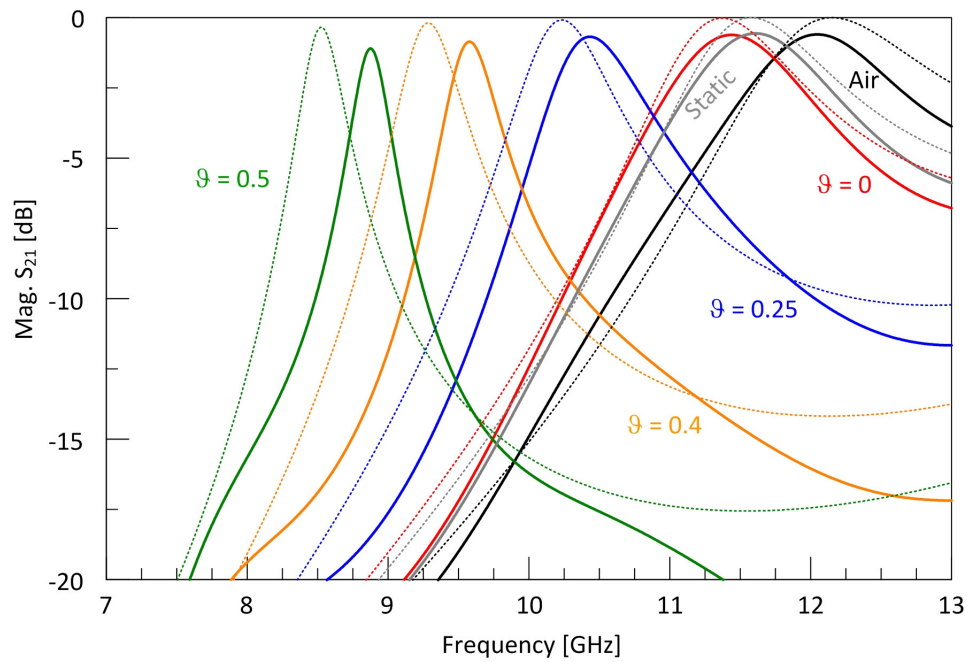


Fig. 22. Circuit model (dotted) and HFSS simulation (solid) predicted S_{21} response for the initial tunable SIW resonator.

The minimum and maximum of S_{11} and S_{21} , respectively, correspond to the resonant frequency for the specified reconfiguration state $f_{0,g}$. The static resonator response is shown as a reference. In a realistic closed-loop system, only dispersions characterized by \mathcal{G} would flow into and out of the dielectric post. However, the response from an air dielectric post easily analyzes the resonators performance without dispersions. Because air has a lower dielectric constant than the substrate, the air dielectric post produces a low-loss material perturbation of the static resonator causing an increase in resonant frequency. As high \mathcal{G} (high dielectric) fluidic dispersions enter the dielectric post, $f_{0,g}$ shifts towards the lower portion of X-band. The resonance points for both circuit model and HFSS simulations are in strong agreement ($< 4\%$ difference), validating the circuit model. Across reconfiguration, the predicted insertion loss (IL) ($-|S_{21}|_{dB}$) remains < 1.1 dB and return loss (RL) ($-|S_{11}|_{dB}$) remains > 19 dB for the HFSS simulation. The higher IL in the HFSS simulation occurs from losses in the microstrip line, tapered transition, and SIW sections transitioning to the resonator. HFSS predicts reconfiguration up to 22.4% at $\mathcal{G} = 0.5$, with the percentage frequency shift from the $\mathcal{G} = 0$ state defined as $\Delta f_{0,g} = |f_{0,0} - f_{0,g}| / f_{0,0}$.

The resonant frequency across reconfiguration states can also be predicted using (3.15) and the result can be used in (3.20) to estimate the unloaded Q of the resonator. A summary of results for the $f_{0,g}$ and Q are shown in Table 4.

Table 4. Summary of $f_{0,g}$ and Q for the initial tunable SIW resonator design.

Dielectric Post State	Resonant Frequency f_0 [GHz]			Quality Factor Q	
	<i>HFSS</i>	<i>Circuit Model</i>	<i>Closed-form Approximation (3.15)</i>	<i>HFSS</i>	<i>Closed-form Approximation (3.20)</i>
Air	12.05	12.15	12.39	580	589
$g = 0$	11.44	11.37	11.48	570	515
$g = 0.25$	10.43	10.24	10.1	524	393
$g = 0.4$	9.57	9.29	8.74	465	286
$g = 0.5$	8.88	8.53	7.39	412	201

The closed-form formulas predict $f_{0,g}$ within 9% of the HFSS simulations up to $g = 0.4$ and air and 16.7% for $g = 0.5$. The closed-form Q differs up to 51.2% from HFSS at $g = 0.5$. The large differences arise because the closed-form formulas assume a much stronger perturbation from the integral approximation in (3.14) and the fact that the quasi-static approximation assumes identical fields in the numerator of (3.13). The most accurate approximations are from HFSS simulations because the physical features of the actual SIW resonator are accounted for.

4.3 Fabrication and Measured Results

The SIW resonator was fabricated using standard printed circuit board techniques. Thru holes were drilled ($d = 1.5113$ mm), plugged with small sections of copper AWG 14 (1.6mm diameter) wire, and soldered to the ground plane and SIW top metallization to create the lateral wall vias and inductive posts. A single thru hole was drilled and thin circuit board wiring was soldered across the openings to create the dielectric post. The thin wire allows fluid to flow into and out of the dielectric post while

maintaining the perturbation within the cavity. SMA connectors were attached at the microstrip line edges providing connectivity to the test equipment. The measured response vs. the HFSS response for the initial SIW resonator along with a picture of the fabricated device is shown in Fig. 23 and Fig. 24. The physical tunable resonator achieves a $\Delta f_{0,g}$ of 20.8% from 11.54 to 9.14 GHz utilizing $0 < g < 0.5$ fluidic dispersions. The resonance points predicted from HFSS differ by less than 4% for all reconfiguration states. The IL and RL (excluding $g = 0.25$) performance of the resonator become significantly worse across reconfiguration ($RL < 10$ dB and $IL > 3$ dB), revealing the possibility that the dispersions contain more losses than expected. However, the air dielectric post (a very low-loss perturbation) produces a ~ 2 dB higher IL than the HFSS prediction. The possibility that the dielectric post behaves as a dielectric resonator antenna (DRA), producing radiation from the post openings, is unlikely. The dimensions of the dielectric post indicate DRA cut-off frequencies of 20 – 70 GHz between the air and $g = 0.5$ reconfiguration cases.

After physically examining the device it was discovered that the SMA connectors were causing significant capacitive loading (Fig. 25). The width of the 50Ω microstrip line W_{50} exceeds the outer diameter of the SMA connector causing metal-air-metal interfaces at the SMA connector-microstrip transition. Although the initial fluidic dispersions appear lossy, this capacitive loading effect invalidates possible conclusions that can be drawn from the measured data.

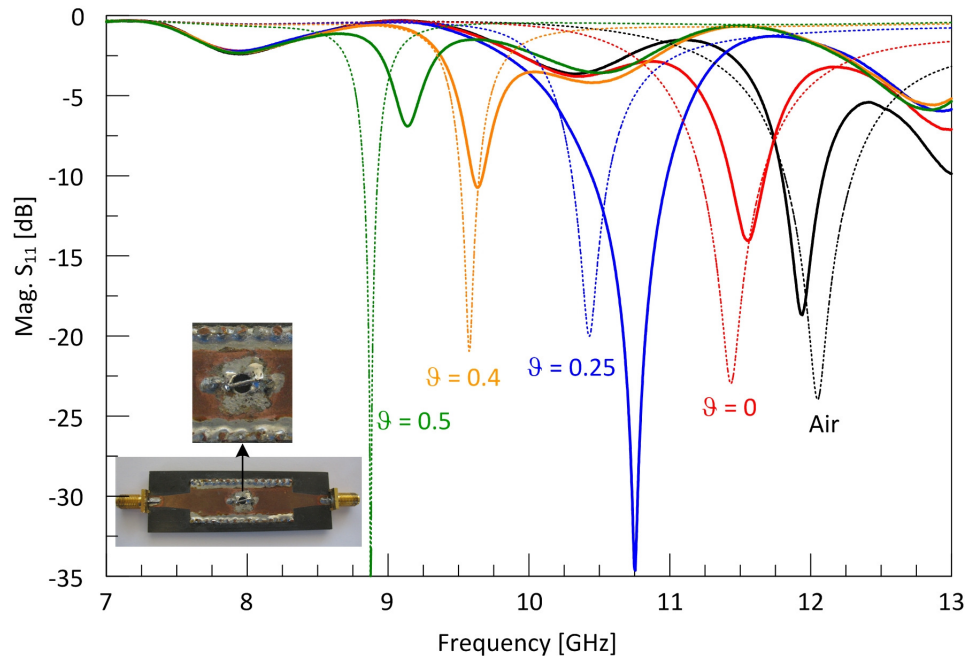


Fig. 23. Measured (solid) and HFSS simulation (dotted) S_{11} response for the initial tunable SIW resonator.

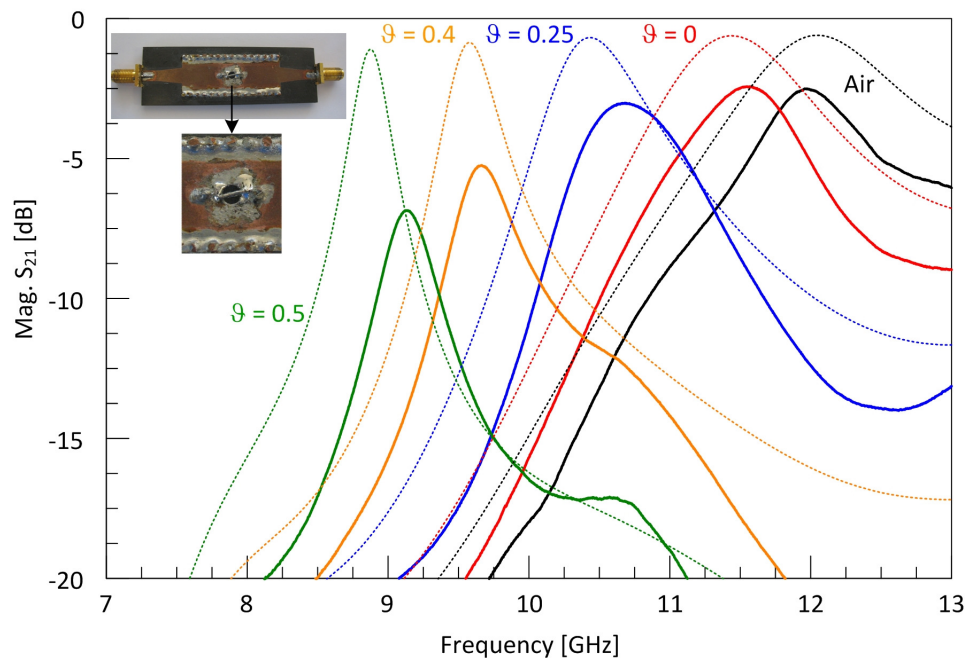


Fig. 24. Measured (solid) and HFSS simulation (dotted) S_{21} response for the initial tunable SIW resonator.

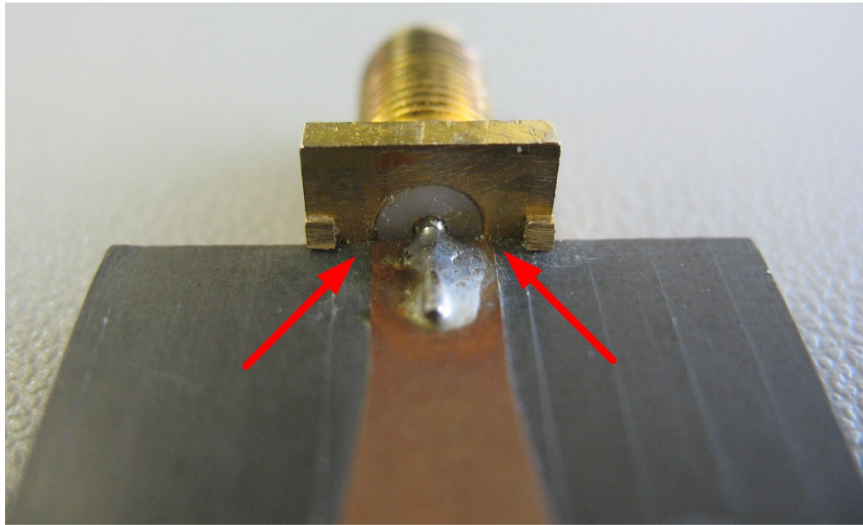


Fig. 25. Capacitive loading effected from the SMA connectors indicated by red arrows.

CHAPTER V

DESIGN ITERATION 2

5.1 Design Changes

Many issues and improvement areas with the initial design were addressed in the 2nd design iteration. To decrease W_{50} below the outer diameter of the SMA connector, a thinner Rogers 5870 board of thickness 0.7874 mm replaces the 5870 board in the initial design of thickness 1.5748 mm (refer to (2.14) for the effect on the line impedance with changing the substrate thickness). The SMA connectors and dielectric post openings are included in the HFSS model to increase the simulation accuracy. The exact dimensions of the SMA connector can be found from the data sheet for the specific supplier. In this work, the dimensions were directly measured off the connectors utilized. A crossed wire structure replaces the single wire structure across the top and bottom of the dielectric post lessening the possibility of radiation. The via diameters used in simulation match the AWG 14 wire (1.6 mm diameter) as opposed to the 1.5113 mm drilled thru holes. The values of W_{tap} and L_{tap} are optimized to provided $S_{11} < -16$ dB (opposed to -10 dB in the initial design) across X-band for the SIW structure. The optimization utilized a Quasi-Newton routine built in HFSS. The complete simulation model for the 2nd SIW resonator is shown in Fig. 26. The new dimensions for the 2nd SIW resonator are given in Table 5.

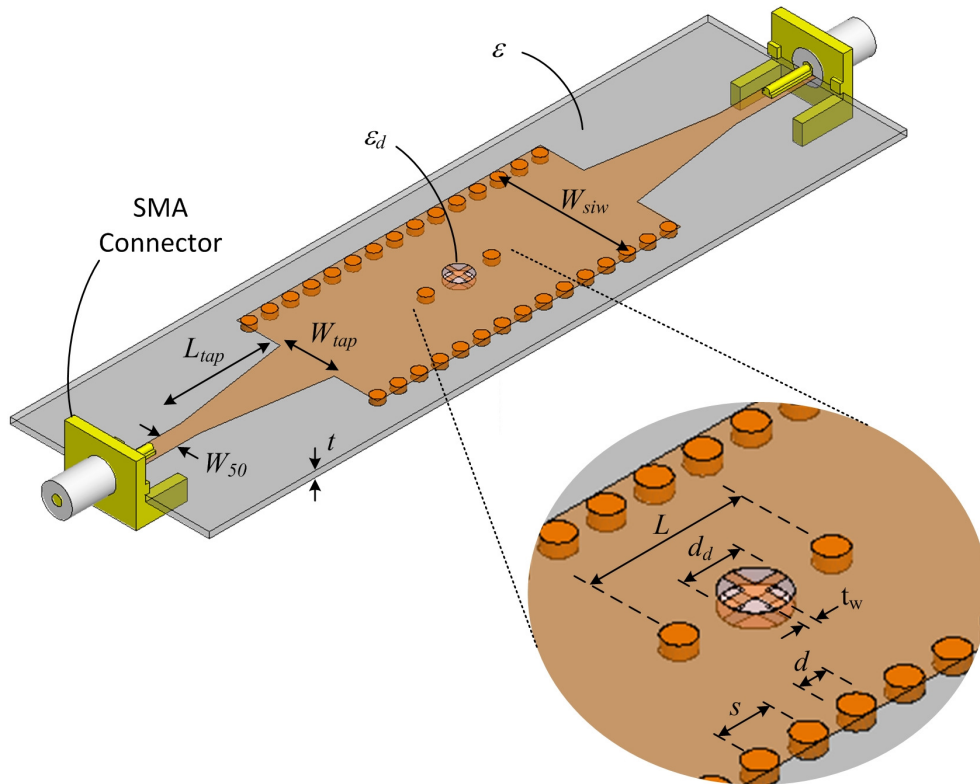


Fig. 26. Complete HFSS simulation model for the 2nd SIW tunable resonator.

Table 5. Dimensions of the 2nd tunable SIW resonator.

Parameter	Dimension (mm)
d	1.6
d_d	3.175
L	8.7
L_{tap}	15.49
s	2.75
t	0.7874
W_{50}	2.34
W_{siw}	17
W_{tap}	7.11
t_w	0.65

5.2 New Dispersions

A new batch of dispersions were created replacing the BSTO particles with Barium Titanate (BTO) particles, same estimated permittivity of $\varepsilon_2/\varepsilon_0 \sim 500(1-j0.05)$. The spherical BTO particles have diameters < 400 nm. A 1000 *cst* SF (providing very stable dispersion across $0 < \vartheta < 0.5$) from a different manufacture replaces the 50 – 1050 *cst* SF used in the initial dispersions. A finer sampling of $\vartheta = 0, 0.1, 0.2, 0.3, 0.4,$ and 0.5 dispersions were mixed. The new dispersions allow comparison against the possibly bad batch of initial dispersions. The MG mixing rule predicts the effective material properties summarized in Table 6.

Table 6. Estimated ε_{eff} for 2nd batch of fluidic dispersions using the MG mixing rule.

ϑ	$\varepsilon_{eff}/\varepsilon_0 = \varepsilon'_{eff}(1-j\tan\delta_{eff})$
0	$2.8(1-j0.001)$
0.1	$3.72(1-j0.0012)$
0.2	$4.86(1-j0.0014)$
0.3	$6.32(1-j0.0016)$
0.4	$8.25(1-j0.0019)$
0.5	$10.93(1-j0.0022)$

5.3 Predicted Performance

The simulated frequency response from HFSS compared to the response from the circuit model is shown in Fig. 27 and Fig. 28.

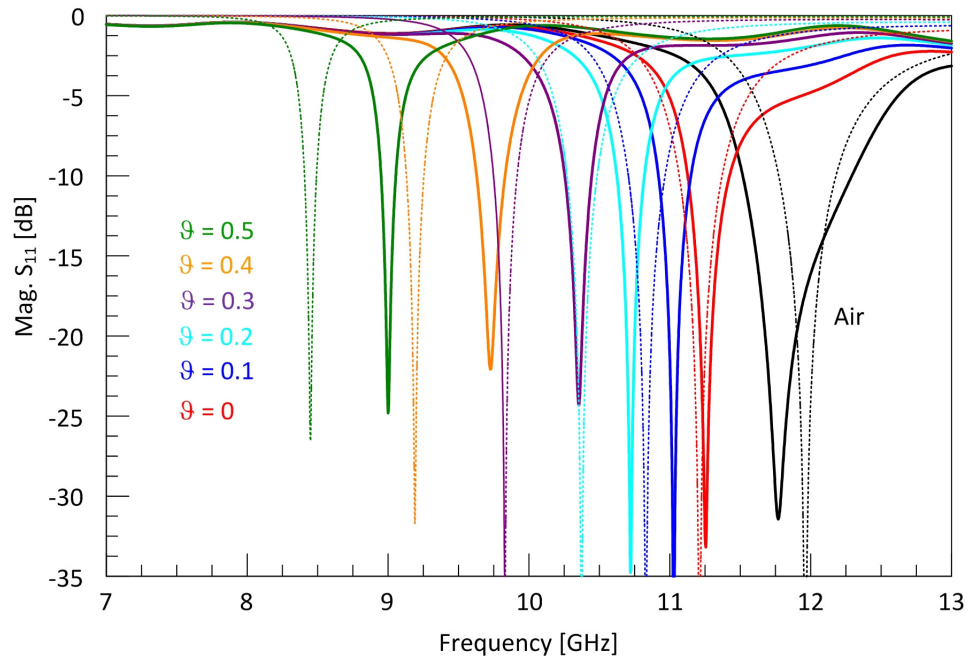


Fig. 27. Circuit model (dotted) and HFSS simulation (solid) predicted S_{11} response for the 2nd tunable SIW resonator.

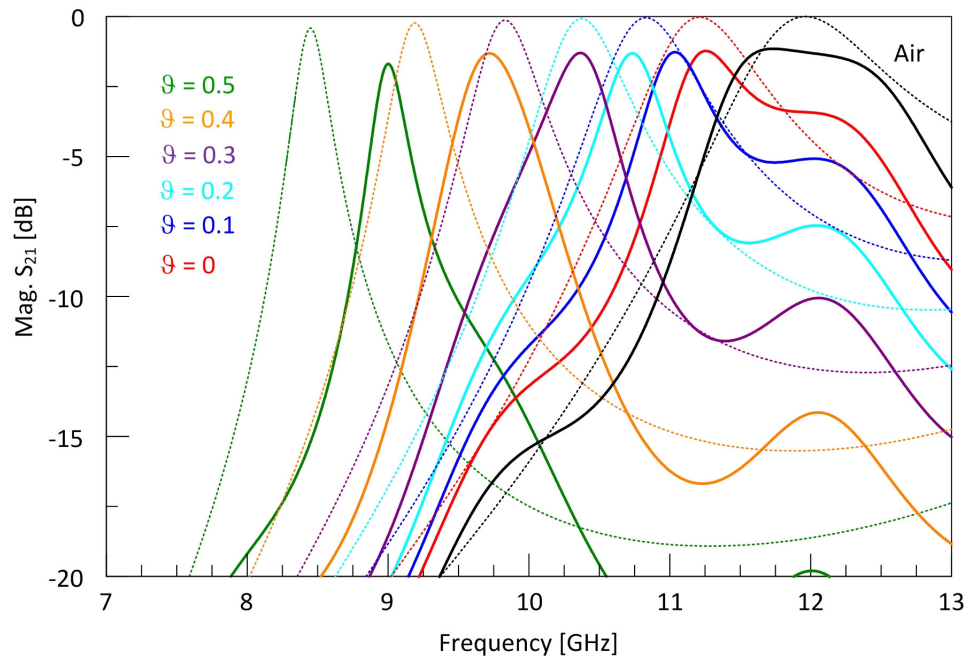


Fig. 28. Circuit model (dotted) and HFSS simulation (solid) predicted S_{21} response for the 2nd tunable SIW resonator.

The openings in the dielectric post accounted for in HFSS (not accounted for in the circuit model) weaken the perturbation effect causing a slightly larger difference in the resonance points ($< 6.2\%$) compared to the initial design ($< 4\%$). Across reconfiguration, the predicted HFSS IL remains < 1.7 dB and RL remains > 20 dB despite the addition of the SMA connector and dielectric post openings. Again, the higher IL and lower RL in the HFSS simulation occur from the microstrip line, tapered transition, and SIW sections loading the resonator. HFSS predicts $\Delta f_{0,g} = 20\%$ reconfiguration at $g = 0.5$, slightly lower than the HFSS prediction for the initial design due to the addition of the dielectric post openings.

Taking the cross-sectional area A of the perturbation in (3.15) as the area of the crossed wires at the dielectric post openings accurately accounts for the weakening of the perturbation effect caused by the dielectric post openings (difficult to account for in the circuit model). With $A = 4.7504 \text{ mm}^2$ (slightly larger than the actual area of the crossed wires to account for fringing fields along the wires) the predicted $f_{0,g}$ and unloaded Q (along with predictions from HFSS and the circuit model) are shown in Table 7. The Q 's predicted from HFSS are lower than the Q 's from the initial design because the thinner substrate material. The differences between HFSS and the closed-form solutions for the resonant frequency and Q are $< 1.16\%$ and $< 10.4\%$, respectively. The closer agreement as compared to the initial design can be attributed to the effective lowering of the perturbation effect with A in (3.15).

Table 7. Summary of $f_{0,g}$ and Q for the 2nd tunable SIW resonator design

Dielectric Post	Resonant Frequency f_0 [GHz]			Quality Factor Q	
	<i>HFSS</i>	<i>Circuit Model</i>	<i>Closed-form Approximation (3.15)</i>	<i>HFSS</i>	<i>Closed-form Approximation (3.20)</i>
Air	11.77	11.96	11.72	469	477
$g = 0$	11.26	11.21	11.21	457	447
$g = 0.1$	11.03	10.83	10.96	445	429
$g = 0.2$	10.72	10.37	10.64	425	406
$g = 0.3$	10.35	9.83	10.23	396	375
$g = 0.4$	9.74	9.19	9.69	356	333
$g = 0.5$	9.0	8.45	8.94	310	278

5.4 Fabrication and Measured Results

The 2nd tunable SIW resonator was fabricated in the same manner as the initial design (Section 4.3). The measured response (tested with the new BTO dispersions) compared to the HFSS response along with a picture of the fabricated device is shown in Fig. 29 and Fig. 30.

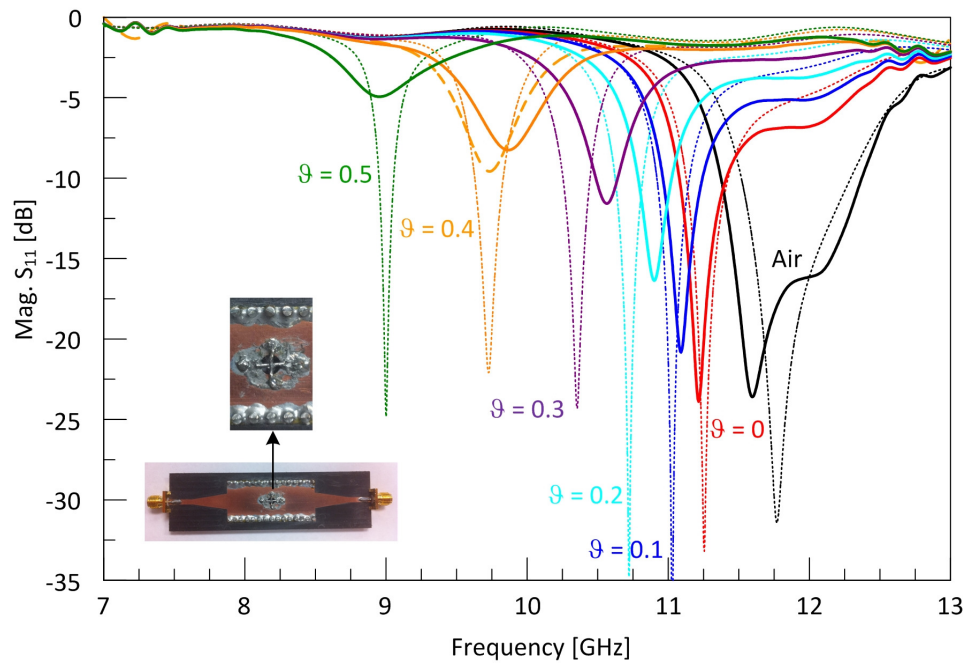


Fig. 29. Measured (solid) and HFSS simulated (dotted) S_{11} response for the 2nd tunable SIW resonator.

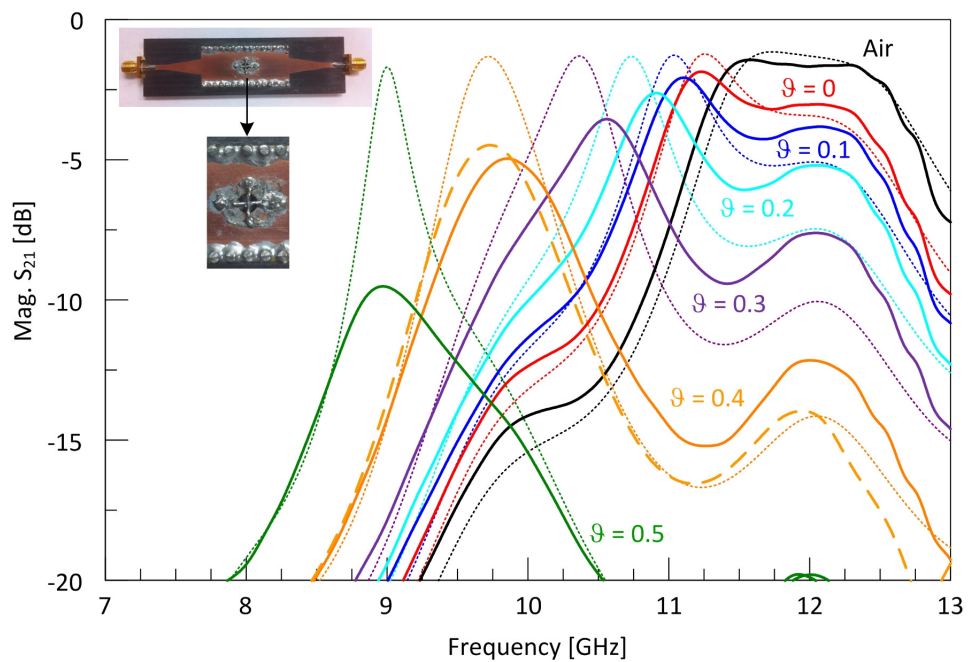


Fig. 30. Measured (solid) and HFSS simulated (dotted) S_{21} response for the 2nd tunable SIW resonator.

The 2nd SIW tunable resonator was also tested with the initial $\vartheta = 0.4$ BSTO dispersion, signified by the orange dashed line in Fig. 29 and Fig. 30. The physical tunable resonator achieves a $\Delta f_{0,\vartheta}$ of 20.42% from 11.22 GHz to 8.93 GHz utilizing $0 < \vartheta < 0.5$ dispersions. The resonance points predicted from HFSS differ by less than 2% for all reconfiguration states. The RL decreases ($RL > 5$ dB) and IL increases ($IL < 10$ dB) as high ϑ fluidic BTO dispersions (including the $\vartheta = 0.4$ BSTO dispersion) are introduced into the dielectric post, as seen in the initial design. However, the air reconfiguration case (a known low-loss perturbation) agrees very well with the HFSS prediction reinforcing the conclusion that the dispersions (both BSTO and BTO batches) may be intrinsically high-loss.

5.5 Material Property Study

The loss of the SF dominates the loss of the dispersion over $0 < \vartheta < 0.5$. A parametric study analyzing $0.01 < \tan\delta_1 < 0.06$ in 0.01 increments was completed in HFSS (Fig. 31 and Fig. 32). The same estimate for the BTO (and BSTO) particles was used in the study.

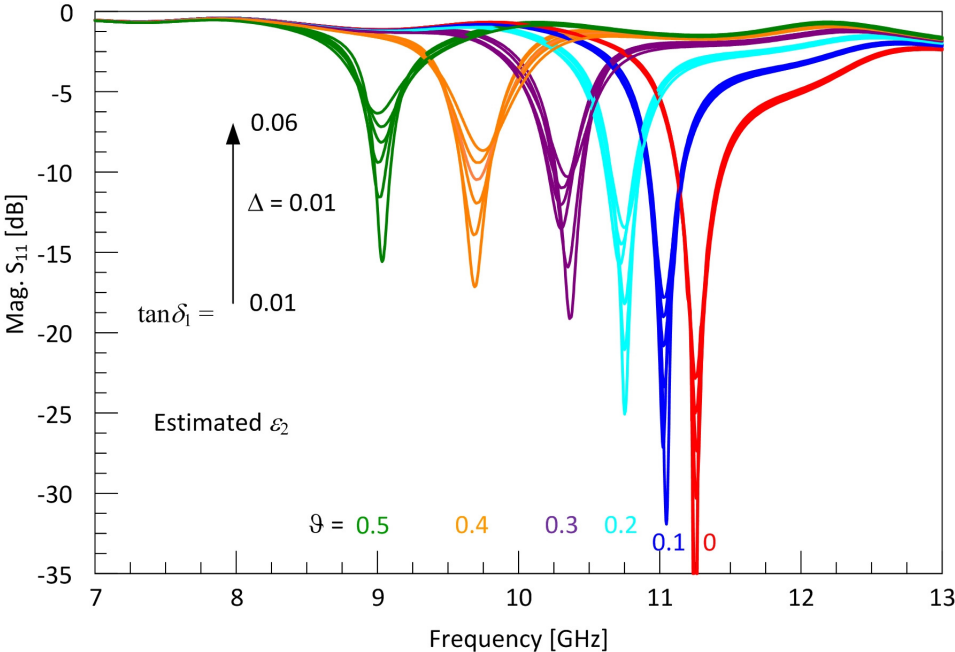


Fig. 31. HFSS simulated S_{11} response for the SF loss tangent parametric study.

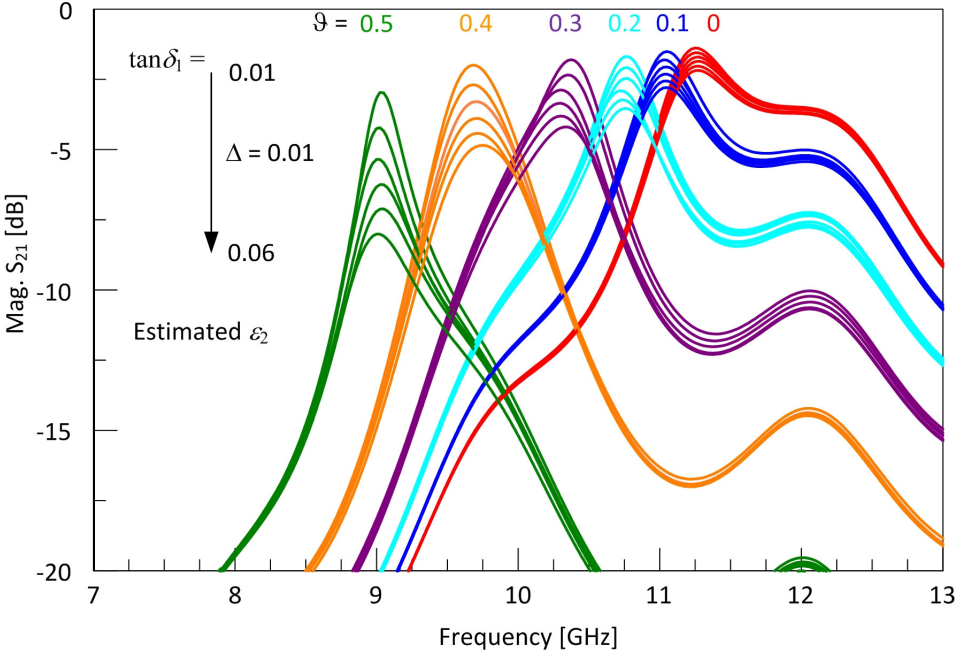


Fig. 32. HFSS simulated S_{21} response for the SF loss tangent parametric study.

A new SF complex permittivity estimate is found to be $\varepsilon_1/\varepsilon_0 \sim 2.8(1-j0.04)$ by comparing the IL and RL of the measured and parametric study for the $\mathcal{G} = 0$ case. The BTO (and BSTO) particles must possess higher losses than expected because high \mathcal{G} cases (with the new SF permittivity estimate) still do not compare to measurement. In order for the losses of the spherical particles to play a role in the fluidic dispersion loss, the value of ε'_2 must decrease according to the MG mixing rule in (2.28). With a new permittivity estimate of $\varepsilon_2/\varepsilon_0 \sim 100(1-j0.5)$ for the BTO (BSTO) particles and the aforementioned new permittivity estimate for the SF, the HFSS response compares to the measured response as shown in Fig. 33 and Fig. 34. Table 8 indicates the new dispersion permittivity estimates.

Table 8. New predicted ε_d for new estimated ε_1 and ε_2 using the MG mixing rule.

\mathcal{G}	$\varepsilon_d/\varepsilon_0 = \varepsilon'_d(1-j\tan\delta_d)$
0	$2.8(1-j0.04)$
0.1	$3.66(1-j0.0479)$
0.2	$4.73(1-j0.0552)$
0.3	$6.06(1-j0.0627)$
0.4	$7.8(1-j0.0711)$
0.5	$10.13(1-j0.0813)$

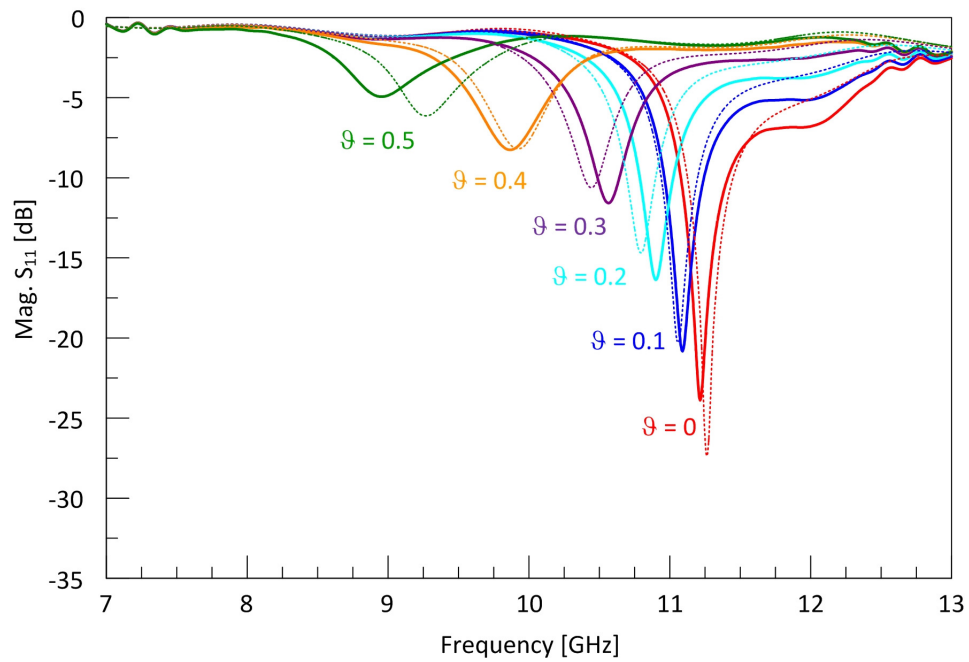


Fig. 33. Measured (solid) and HFSS simulated (dotted) S_{11} response for the 2nd tunable SIW resonator with new estimated fluidic dispersion permittivity.

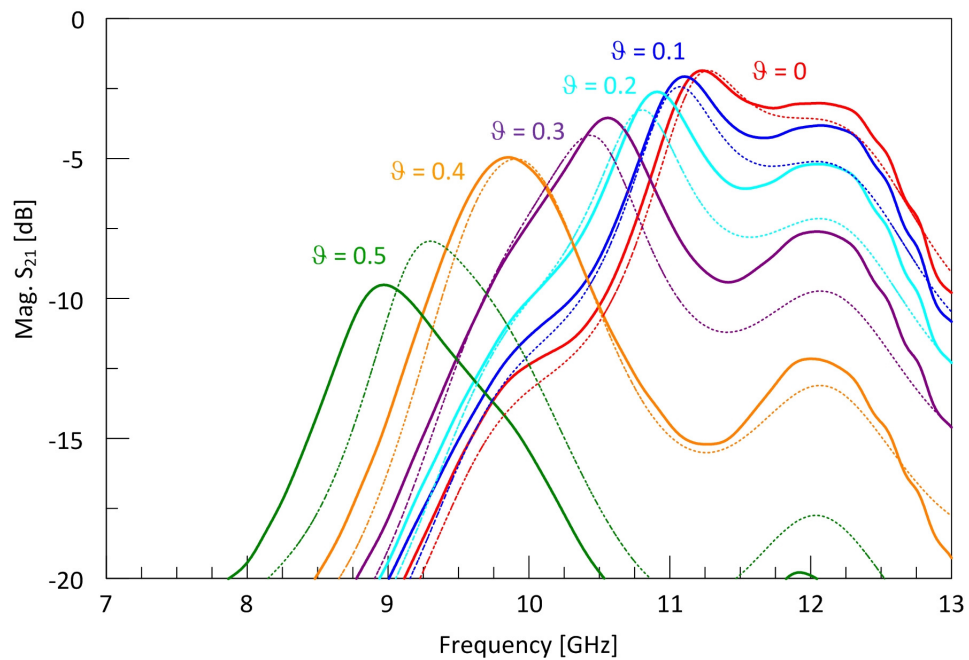


Fig. 34. Measured (solid) and HFSS simulated (dotted) S_{21} response for the 2nd tunable SIW resonator with new estimated fluidic dispersion permittivity.

The resonance points differ by less than 4% despite the significant drop in the new ϵ'_2 estimate because the dominate SF properties in the fluidic dispersions. The strong correlation between simulated and measured RL and IL validates the new estimated SF and BTO (BSTO) complex permittivity.

The predicted response from the circuit model with the new fluidic dispersion permittivity estimate vs. the measure response is shown in Fig. 35 and Fig. 36. The circuit model predicts stronger frequency shifts since the dielectric post openings are not considered. The difference in resonance points between the measured and circuit model response remains low ($< 6\%$). The circuit model reflects the increase in IL and decrease in RL for higher θ cases from the measured device. The higher measured IL for all reconfiguration cases can be attributed to the conduction losses from the copper vias and metallization layers, and loading from the microstrip line, tapered transition, and SIW sections. The strong correlations between the circuit model (no openings in the dielectric post accounted for) compared to the measured response proves little radiation occurs from the openings in the dielectric post.

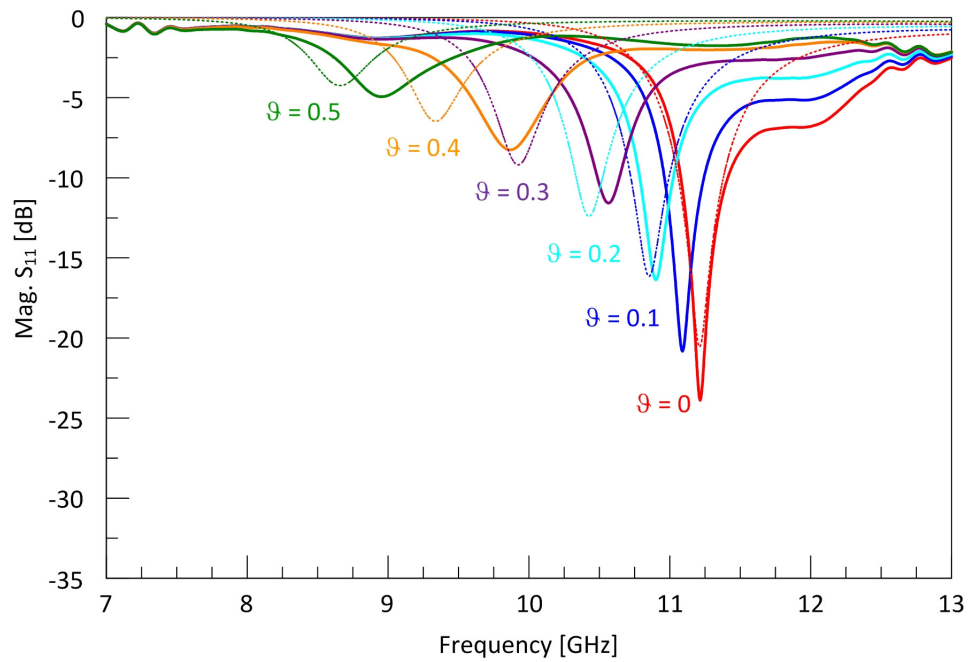


Fig. 35. Measured (solid) and circuit model (dotted) S_{11} response for the 2nd tunable SIW resonator with new estimated fluidic dispersion permittivity.

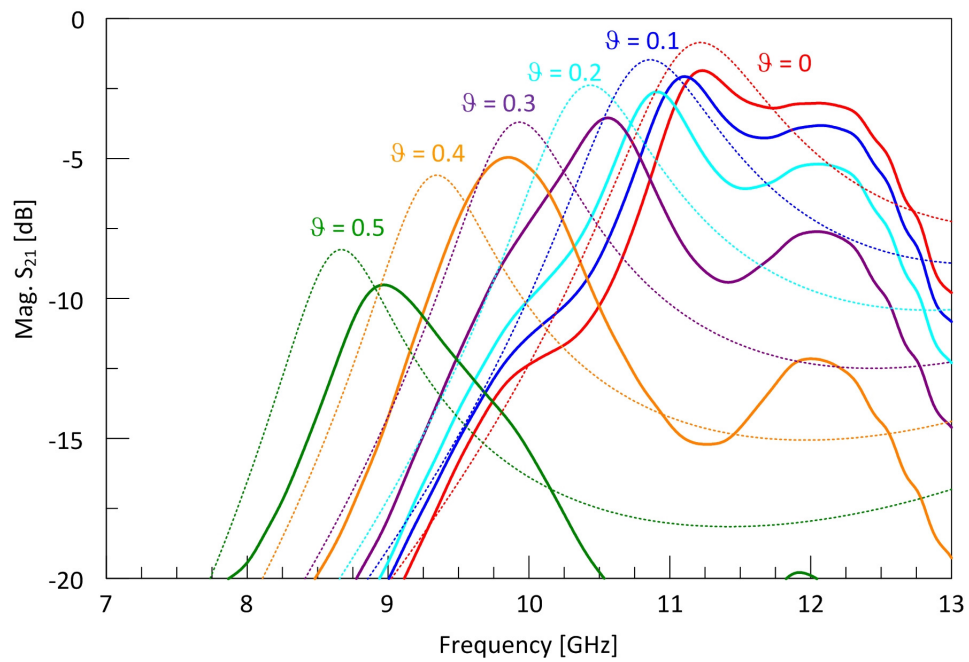


Fig. 36. Measured (solid) and circuit model (dotted) S_{21} response for the 2nd tunable SIW resonator with new estimated fluidic dispersion permittivity.

The predicted unloaded Q 's for the resonator using the new permittivity estimates are given in Table 9. The closed-form estimates strongly agree with full-wave simulation. The high-loss dispersions significantly decrease the Q of the tunable SIW resonator (100s to 10s).

Table 9. Predicted tunable SIW resonator Q with new estimated fluidic dispersion permittivity.

\mathcal{D}	HFSS	(3.20)
0	134	130
0.1	89	90
0.2	60	63
0.3	41	44
0.4	28	30
0.5	20	19

5.6 Discussion and Conclusion

The low RL occurring as high \mathcal{D} dispersions enter the dielectric post manifests as the circuit components (Fig. 17) become both reactive and resistive. The resistive elements alter the input impedance of the resonator creating an impedance mismatch. The high IL is partially due to the lower RL, but mainly occurs from dissipation caused by the high-loss dispersions in the resonator. The percentage of dissipated energy in the resonator can be computed as

$$\alpha = 1 - |S_{11}|^2 - |S_{21}|^2. \quad (5.1)$$

The energy lost from high-loss dispersions at resonance across reconfiguration from the circuit model, HFSS, and measurement are shown in Table 10. Significantly more dissipation occurs (lowering the Q of the resonator) for high \mathcal{G} dispersion.

Table 10. Tunable SIW resonator dissipation α with the new estimated fluidic dispersion permittivity.

\mathcal{G}	Circuit Model	HFSS	Measured
0	17.1 %	34.52 %	34.64 %
0.1	26.37 %	42.36 %	37.36 %
0.2	36.49 %	49.56 %	43.07 %
0.3	45.36 %	53.08 %	48.81 %
0.4	49.89 %	53.37 %	53.09 %
0.5	47.44 %	59.76 %	56.62 %

After an exhaustive literature search, the dielectric properties of SF were found to be $\varepsilon_1/\varepsilon_0 \sim 2.7(1-j0.02)$ at X-band frequencies in [24] and $\varepsilon_1/\varepsilon_0 \sim 2.68(1-j0.039)$ between 72 and 82 GHz in [25]. The prediction of $\varepsilon_1/\varepsilon_0 \sim 2.8(1-j0.04)$ from the SIW resonator follows the general measurements in literature. No significant measurements for BSTO or BTO above 1 MHz were found by the author.

Through extensive testing and analysis completed over two design iterations, the performance of the tunable SIW resonator suffers from sensitivity to high fluidic dispersion losses. For applications requiring $RL > 8$ dB and $IL < 6$ dB, the current tunable SIW resonator (with current fluidic dispersions) can achieve up to $\Delta f_{0,\mathcal{G}} = 12.1$ % (for $\mathcal{G} \leq 0.3$). Utilizing low-loss dispersions will offer exceptional reconfiguration performance, prompting research for low-loss fluidic microwave material. A new

estimate for the material properties of SF, BSTO, and BTO at X-band frequencies was found by comparing simulated and measured data. A more accurate form of material measurements capable of dynamically measuring the permittivity of a fluidic dispersion in a closed-loop system would accelerate research efforts in finding low-loss variable fluidic dispersions.

CHAPTER VI

MATERIAL MEASUREMENTS

6.1 Overview

In the previous chapter it was found that the fluidic dispersions utilized in this work possessed higher losses than originally expected deteriorating the tunable SIW resonator performance across reconfiguration. Although new estimates for the materials composing the fluidic dispersions were discovered by comparing simulated and measured data, a system tailored to material property characterization expands research efforts to finding low-loss fluidic dispersions. Two initial measurement systems were fabricated to test both solid and liquid samples. Data processing techniques are developed to extract the permittivity of the sample from measured data.

A variety of material measurement systems (MMSs) exist possessing advantages and disadvantages over one another. A measurement technique, either reflection/transmission or resonant, describes a specific MMS. Many factors associated with the material under test (MUT) such as, form and shape, low-loss or high-loss, and dielectric or magnetic determine the type of MMS used. Most materials are dispersive, material properties vary with frequency, making the measurement frequency range of interest. Fig. 37 shows commercially available MMS taken from [26].

Measurement Techniques

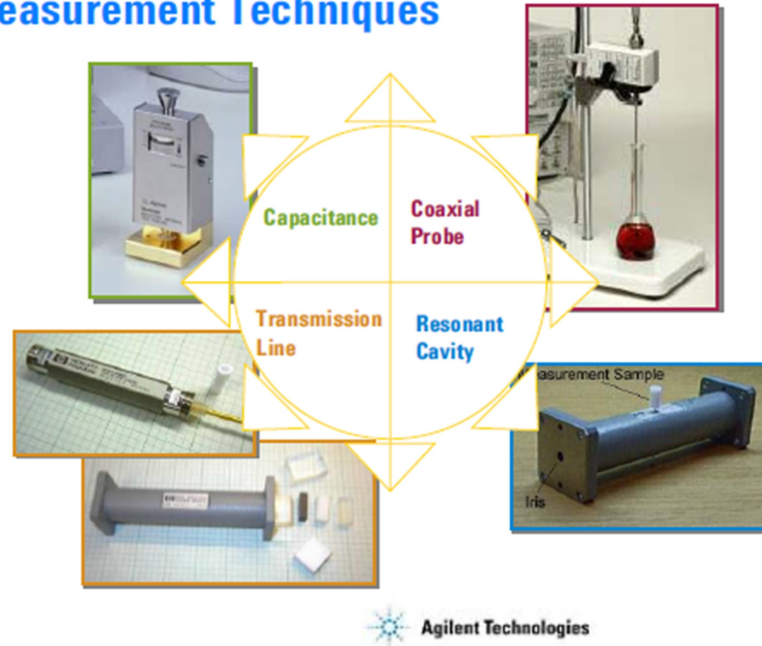


Fig. 37. Commercially available MMSs.

The capacitance MMS typically measures the material properties at low frequencies (< 1 GHz) with an impedance analyzer. The coaxial probe (open-ended) and transmission line (TL) MMS illustrate examples of reflection/transmission measurement techniques. The open-ended coaxial probe (OCP) can measure liquid samples over a large frequency range, however suffers from low accuracy. The TL MMS provides higher accuracy than the OCP; however, the MUT must often be shaped to fit in the fixture. The resonant cavity MMS, a resonant technique, provides the most accuracy but the measurement bandwidth is narrow and the sample size must be tailored to fit in the fixture. The high cost of the commercially available MMSs along with their data processing software limits their uses in academia.

6.2 Initial Low Cost Test Fixtures

Two low cost transmission technique MMS were fabricated to develop data processing methods. A coaxial fixture MMS (CF-MMS) capable of statically measuring liquids is shown in Fig. 38. The thru hole diameter matches the outer diameter of the SMA connector. Tapped holes securely connected the SMA connector to the Aluminum (Al) block. A brass tube links the SMA inner conductors. Fig. 39 demonstrates the assembly of the CF-MMS. The liquid sample can be added to the thru hole cavity in step 2. Thus, the sample becomes the dielectric material of the coaxial line in the Al block. The coaxial structure supports TEM propagation through the sample material. The SMA connectors link to a network analyzer to measure the reflected and transmitted waves from and through the sample, respectively.

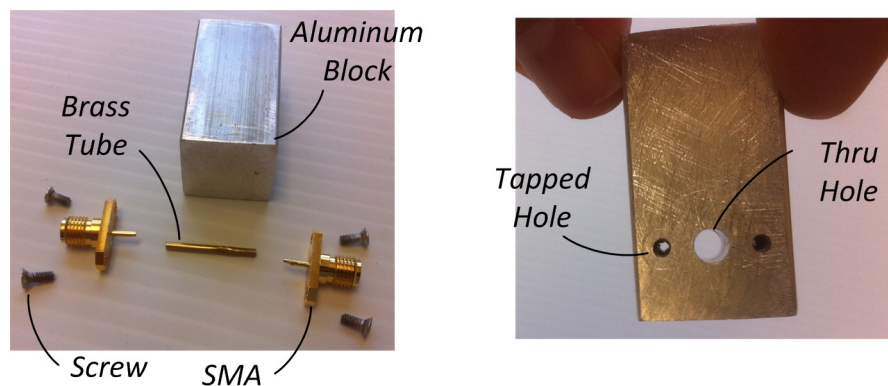


Fig. 38. CF-MMS for measuring liquid samples.

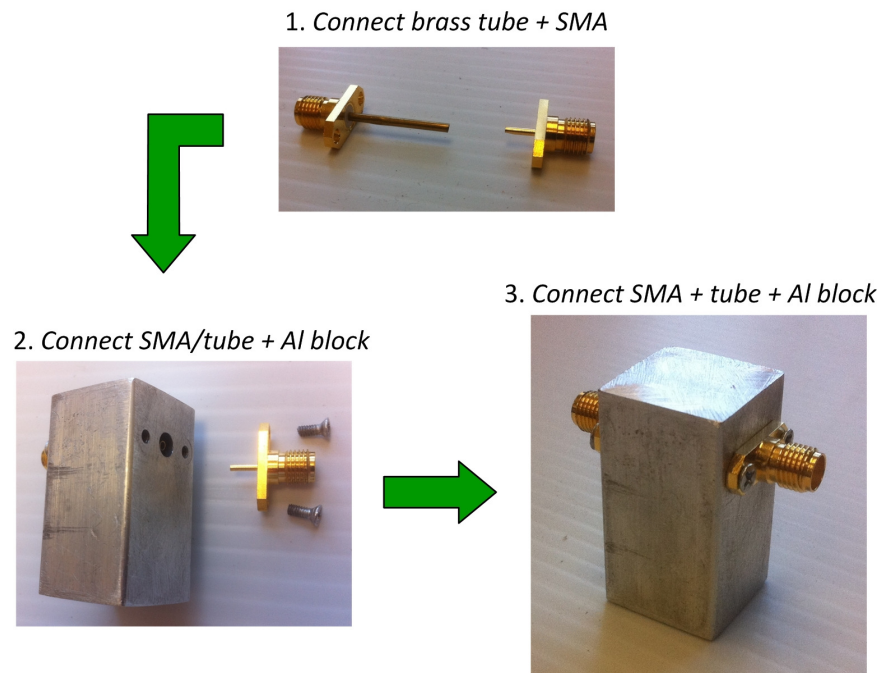


Fig. 39. Assembly procedure for the CF-MMS.

A free-space MMS (FS-MMS) capable of measuring solid and semi-solid materials is shown in Fig. 40. The integrate wheels under the FS-MSS provides effortless mobility. The adjustable MUT holder accommodates flat, planar samples of solid and semi-solid material. Standard gain horn (SGH) antennas connected to a programmable network analyzer (PNA) measure the reflected and transmitted TEM waves from and through the MUT. Fig. 41 shows the basic radiations characteristics of a SGH. The half power beam width θ_{HPBW} defines the area of maximum radiation normal to the SGH aperture. The far-field radiation zone supports TEM propagation. The MUT holder and top SGH can be vertically adjusted to control the distance between the MUT face and SGH aperture. This ensures the MUT lies in the far-field radiation zone and receives as much radiation as possible.

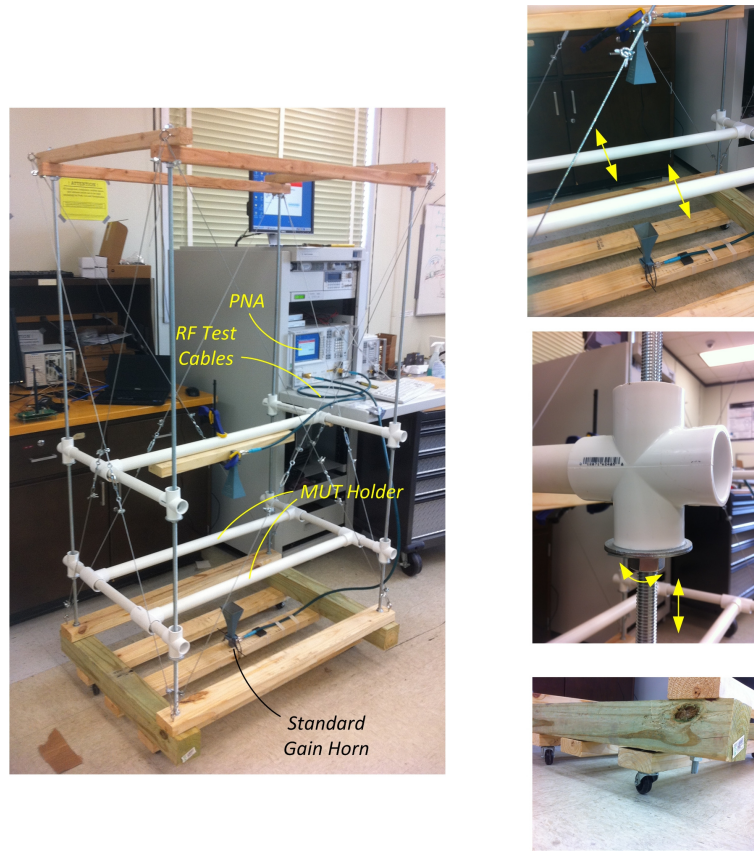


Fig. 40. FS-MMS capable of measuring solids and semi-solid materials.

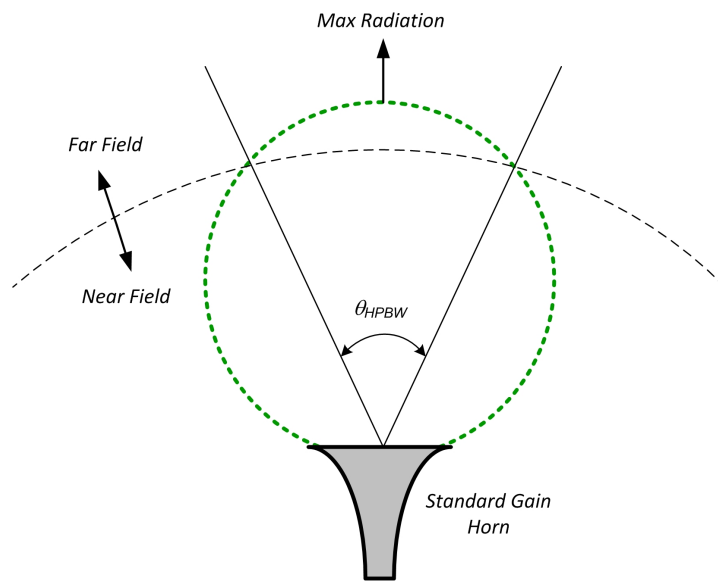


Fig. 41. Radiation characteristics of a SGH antenna.

6.3 Calculation of Complex Dielectric Constant

The CF- and FS-MMS allow a PNA to measure the reflected and transmitted TEM waves from and through an MUT, respectively. The S parameters measured from the PNA pass through data processing software extracting the MUT's complex material properties (μ_s, ε_s). The block diagram in Fig. 42 illustrates the entire system workings.

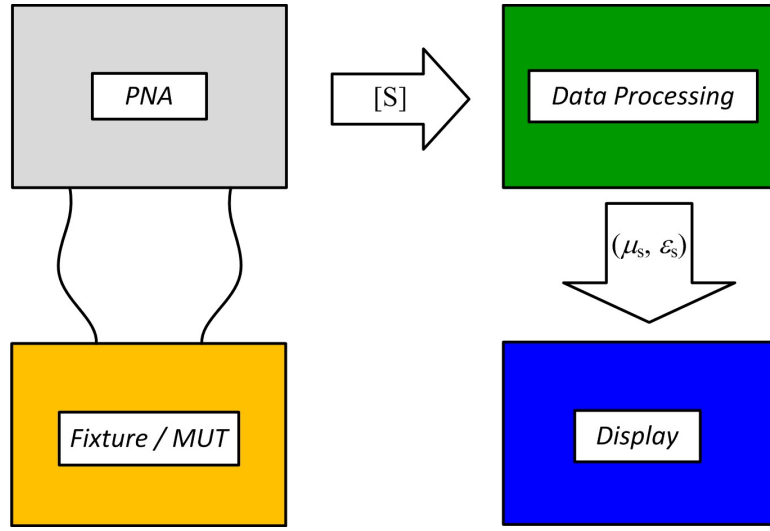


Fig. 42. Block diagram for the MMSs.

In order to extract the (μ_s, ε_s) from the S parameters, consider a TEM wave incident wave on the MUT (thickness d) and the reflected and transmitted energy along with the TL equivalent circuit shown in Fig. 43. Following the techniques from [27], the reflection coefficient at first MUT boundary is,

$$\Gamma_1 = \frac{Z_s - Z}{Z_s + Z} = \frac{z_s - z}{z_s + z} \quad (6.1)$$

where $z_s = Z_s/Z_0$ and $z = Z/Z_0$.

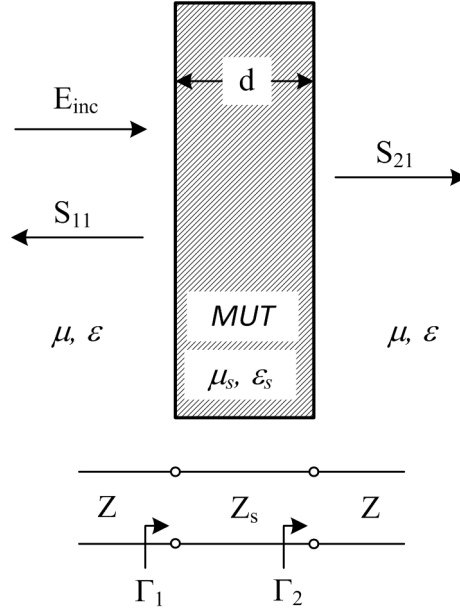


Fig. 43. Diagram of incidence, reflection, and transmission from the MUT and TL equivalent circuit.

The normalized TL equivalent characteristic impedances are thus

$$z_s = \sqrt{\frac{\mu_{rs}}{\epsilon_{rs}}} \quad (6.2)$$

$$z = \sqrt{\frac{\mu_r}{\epsilon_r}}$$

From symmetry, $\Gamma_2 = -\Gamma_1$. The transmission coefficient through the MUT can be defined as,

$$T = e^{-jk_s d} = e^{-jk_0 \sqrt{\epsilon_{rs} \mu_{rs}} d} = e^{-j \frac{2\pi}{\lambda_0} \sqrt{\epsilon_{rs} \mu_{rs}} d}, \quad (6.3)$$

where λ_0 signifies the free-space wavelength. Fig. 44 outlines the signal flow graph formulation from the reflections and transmissions off the MUT boundaries. The right hand side of Fig. 44 depicts the equivalent fields bouncing off the MUT boundaries. The decomposed signal flow graph (Fig. 45) can be solved using the rules in [2].

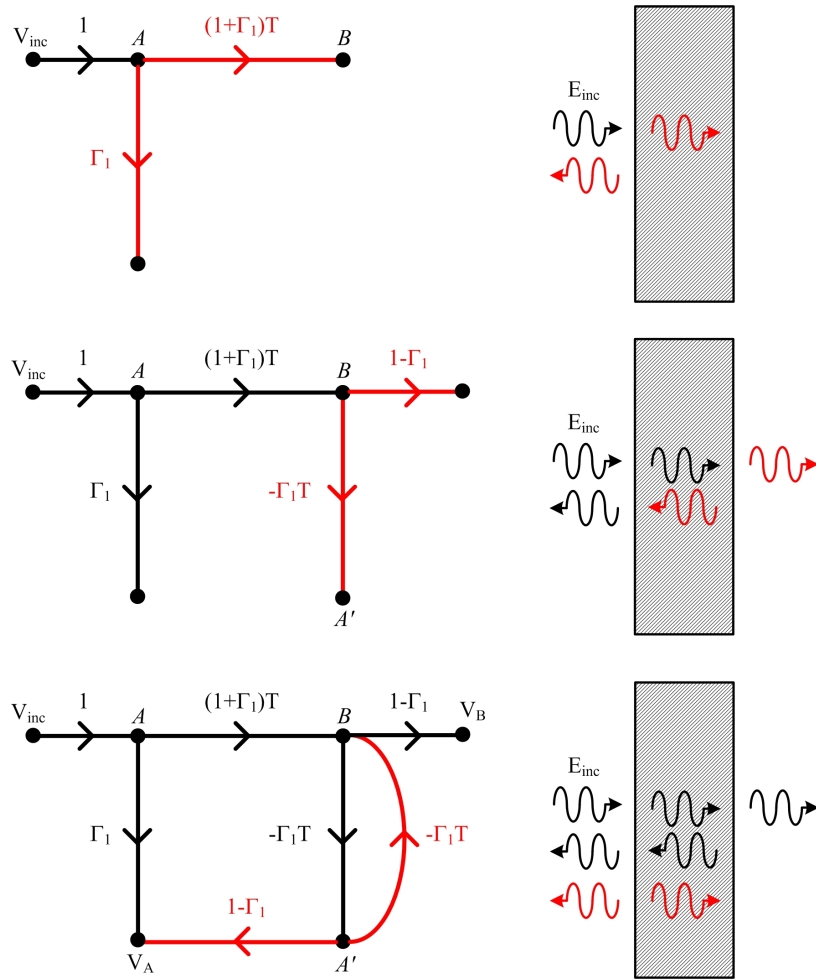


Fig. 44. Signal flow graph formulation for the reflections and transmissions off the MUT boundaries

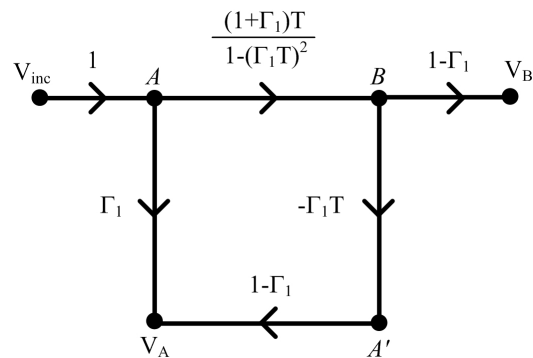


Fig. 45. Decomposed signal flow graph for the reflections and transmissions off the MUT boundaries.

Using the relationship between the nodes and branches of the signal flow graph [2], the S parameters can be solve as

$$S_{11} = \frac{V_a}{V_{inc}} = \frac{(1-T^2)\Gamma_1}{1-(\Gamma_1 T)^2}, \quad (6.4)$$

$$S_{21} = \frac{V_b}{V_{inc}} = \frac{(1-\Gamma_1^2)T}{1-(\Gamma_1 T)^2}. \quad (6.5)$$

The formulation of (6.4) and (6.5) may appear to account for only one round trip of reflections and transmissions through the MUT. However, taking the Maclaurin series of the denominator in (6.4) and (6.5) yields

$$\begin{aligned} S_{11} &= (1-T^2)\Gamma_1 \left[1 + (\Gamma_1 T)^2 + (\Gamma_1 T)^4 + (\Gamma_1 T)^6 + \dots \right] \\ &= \Gamma_1 + (\Gamma_1^2 - 1)\Gamma_1 T^2 + (\Gamma_1^2 - 1)\Gamma_1^3 T^4 + \dots \end{aligned} \quad (6.6)$$

$$\begin{aligned} S_{21} &= (1-\Gamma_1^2)T \left[1 + (\Gamma_1 T)^2 + (\Gamma_1 T)^4 + \dots \right] \\ &= (1-\Gamma_1^2)T + (1-\Gamma_1^2)\Gamma_1^2 T^3 + (1-\Gamma_1^2)\Gamma_1^4 T^5 \dots \end{aligned} \quad (6.7)$$

Fig. 46 shows the complete diagram of reflections and transmission through the MUT. The first terms in (6.6) and (6.7) correspond to the initial reflection and initial transmission of one trip through the sample, respectively. The following terms in (6.6) and (6.7) refer to the subsequent reflections and transmission on the MUT boundaries. Therefore, (6.6) and (6.7) are the superposition of all reflections and transmission due to bounces of the MUT boundaries. The physics of the problem become clear.

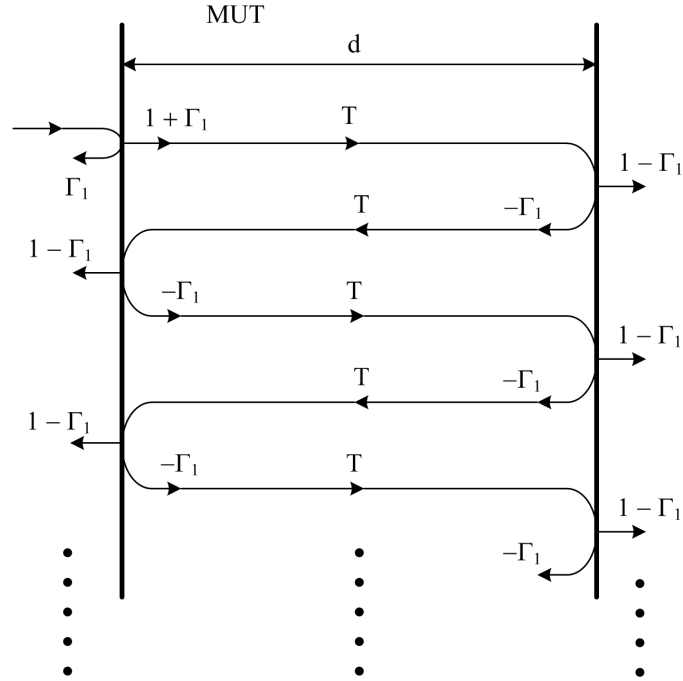


Fig. 46. Complete reflection and transmission diagram off and through the MUT.

If $\mu_{rs} = 1$, then only S_{11} or S_{21} needs to be measured to compute ε_{rs} . An accurate measurement of S_{11} requires sophisticated calibration techniques, a burdensome approach. S_{21} can be accurately measured using a THRU calibration, one of the simplest forms of calibration. Defining S_{21}^c as the RHS of (6.5) and S_{21}^m as the measured S_{21} , an error function can be expressed as

$$E(\varepsilon_{rs}) = |S_{21}^c - S_{21}^m| \quad (6.8)$$

Muller's method (rigorously formed in Appendix A) can be used to numerically compute the complex roots ε_{rs}^c of the function $E(\varepsilon_{rs})$ as in [28].

6.4 Data Processing

Fig. 47 displays a block diagram of the data processing code written in Matlab. The calibration for the FS-MMS places the reference plane directly in the center of the MUT. Thus, the FS-MMS reference plane data must be shifted by

$$S_{21}^m = e^{-j\frac{\pi d}{\lambda_0}} S_{21}^c e^{-j\frac{\pi d}{\lambda_0}}. \quad (6.9)$$

Multiple ϵ_{rs}^c solutions exist when solving (6.8) due to the periodic nature of wave propagation through the MUT. In order to validate if the correct ϵ_{rs} solution is found, the average ϵ_{rs}^c over the measurement frequency range is substituted into (6.5) to compute the expected response. If the measured response matches the expected response over the measured frequency range, then the correct ϵ_{rs}^c solution was found. Appendix B gives the complete Matlab code used in data processing.

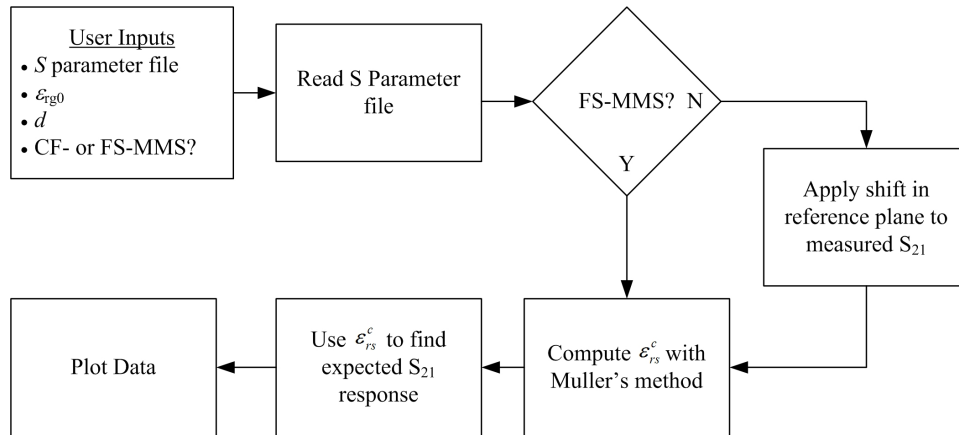


Fig. 47. Block diagram of the data processing code.

6.5 Free-Space MMS Initial Testing

An important feature on the PNA utilized during testing with the FS-MMS is time-domain gating. The PNA allows users to view the time-domain response by taking the Fourier Transform of the frequency response. The time-domain response can then be gated (windowing) to eliminate unwanted reflections/transmissions that occurred during testing. The gated time-domain response is then transformed back into the frequency domain. A sample of known permittivity fine tunes data processing techniques and tests the limitations of the fabricated FS-MMS at X-band frequencies. A large sheet (24" × 20") of Plexiglas, $\epsilon_r = 2.59(1 - j0.0067)$ [24], spanning the dimensions of the FS-MMS was tested (Fig. 48). The measured average dielectric constant differs from the literature value by < 1.5 %. The constant value across X-band for the measured dielectric constant indicates Plexiglas resembles a non-dispersive material at the frequency band, as expected. The average measured loss tangent across X-band differs by ± 0.0015 . The wide variance in measured loss tangent indicates the FS-MMS cannot measure loss accurately, likely due to diffractions and reflections not eliminated from gating. The measured S_{21} response along with the expected response from the calculated dielectric show good agreement. The original phase shift, with no shift in reference plane, is also shown in Fig. 48.

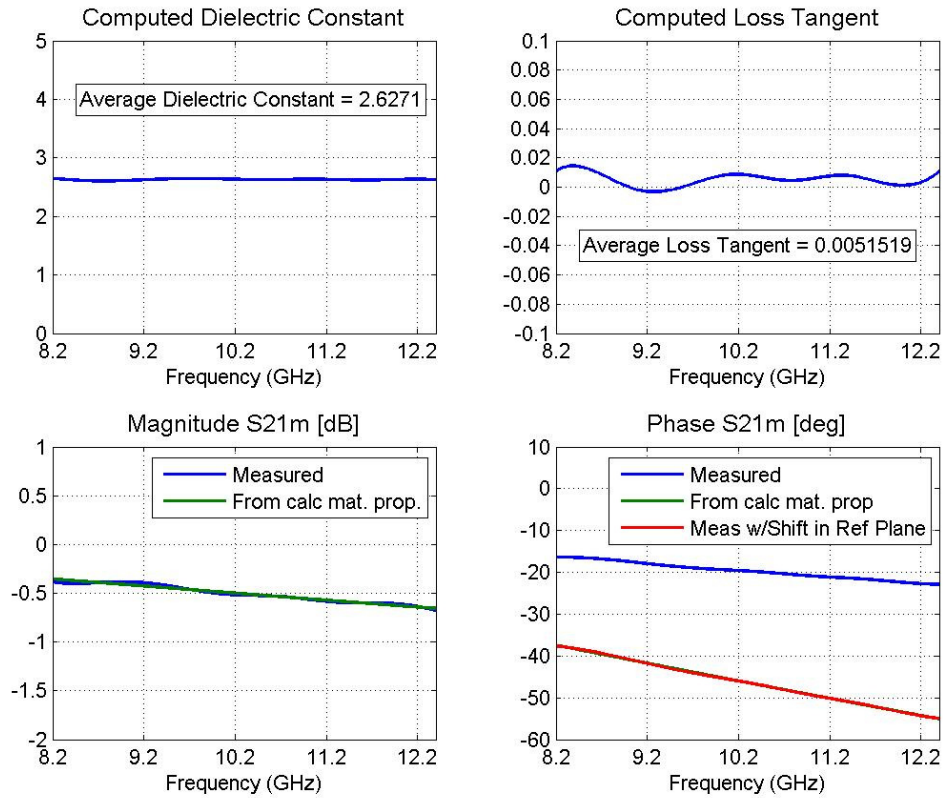


Fig. 48. Large Plexiglas sample measurement results using the FS-MMS.

A measurement taken on small Plexiglas sample (12" × 6") reveals the inaccuracy of the FS-MMS for small sample testing (Fig. 49). Significant diffractions off the edges of the smaller sample severely degraded accuracy. The loss tangent accuracy suffers more heavily than the dielectric constant accuracy.

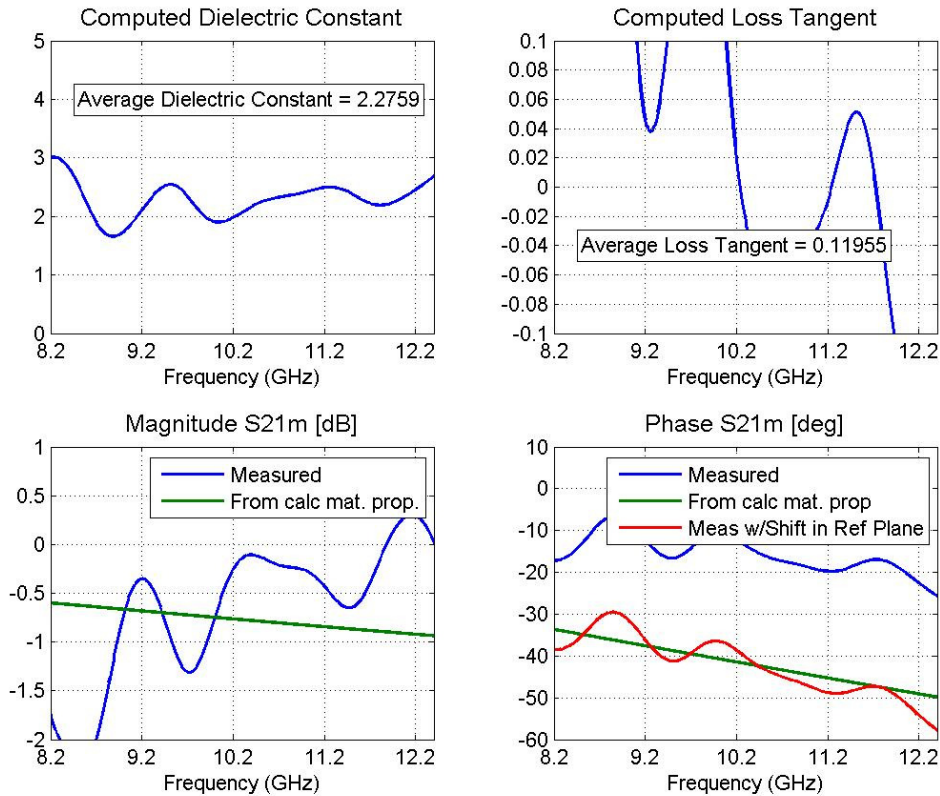


Fig. 49. Small Plexiglas sample measurement results using the FS-MMS.

6.6 Free-Space MMS Small Sample Testing

A technique employed to increase the accuracy of small sample testing for the FS-MMS utilizes a small sample MUT holder. A metal sheet with a 5" \times 5" slot cut in the center creates the holder. Calibration with the holder in place removes the holder from the measurement. The results from the initial test are shown in Fig. 50. The accuracy of the dielectric constant improves while the loss tangent accuracy remains low, although improved.

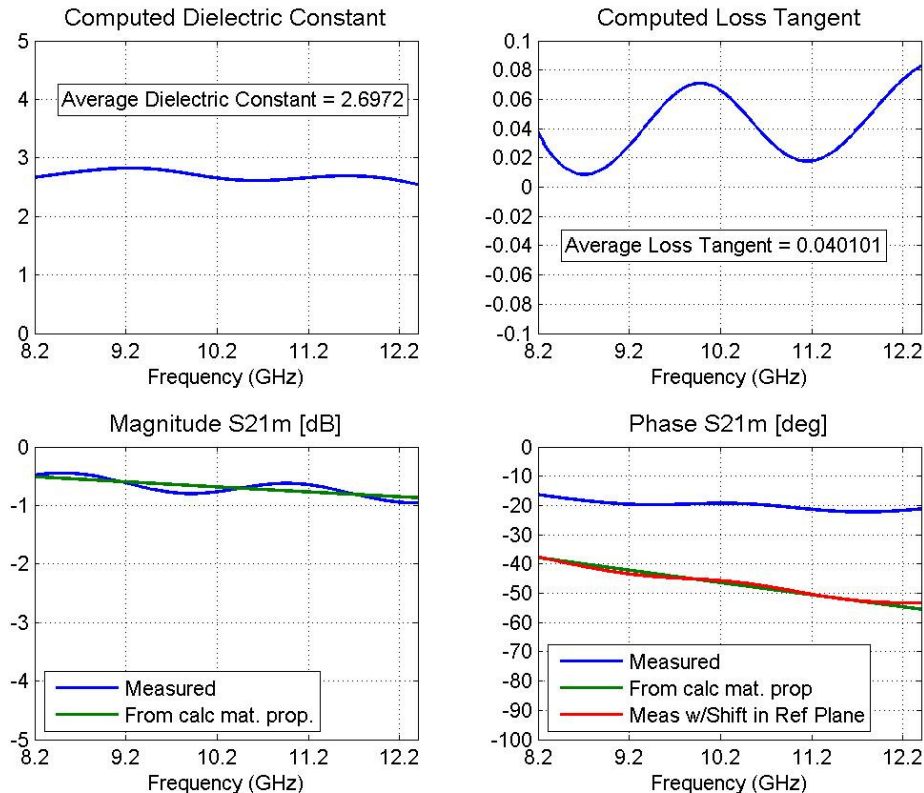


Fig. 50. Small Plexiglas sample measurement results using the FS-MMS with a small sample MUT holder.

6.7 Coaxial Fixture MMS Initial Testing

An SMA barrel of similar length to the SMA probes calibrates the SMA probes out of the measurement. An air sample can be easily measured to test the accuracy of the CF-MMS. The SMA connectors limit the frequency range of the test to below 18 GHz. The testing results are shown in Fig. 51. For very-low frequencies, the accuracy of the dielectric constant heavily degrades. Consistent and expected dielectric constant measurements above 6 GHz indicate the accuracy range for CF-MMS. The crude fabrication of the CF-MMS caused the low accuracy of the loss tangent measurement.

One aspects of the CF-MSS impacting the loss tangent measurement is the connection of the inner conductor via brass tubing possibly causing significant reflections.

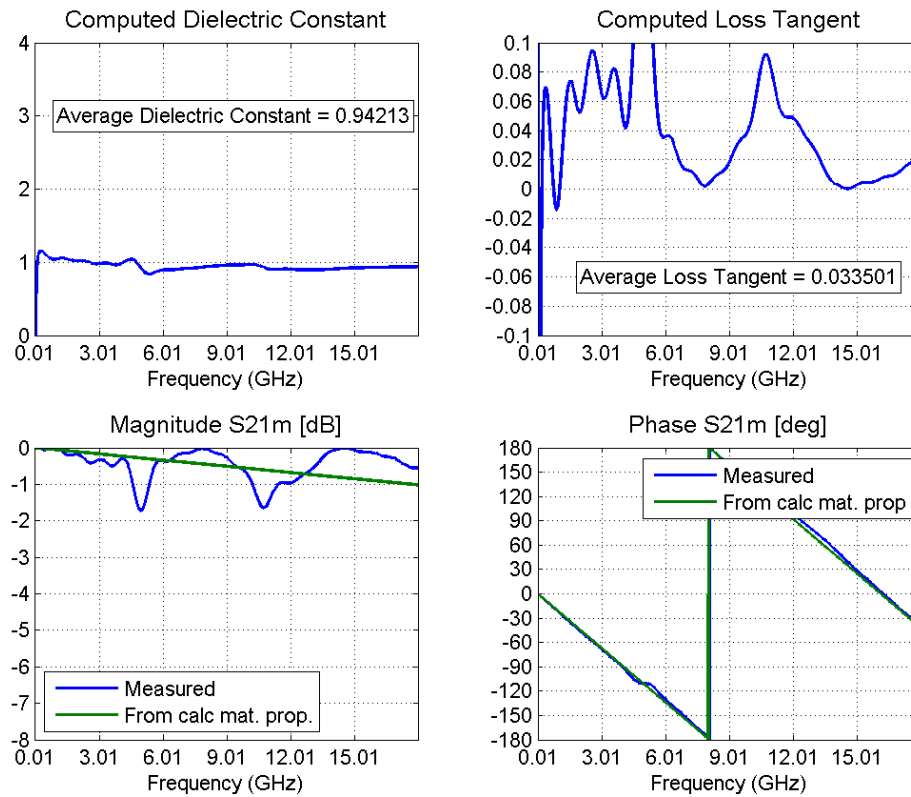


Fig. 51. Air sample measurement results using the CF-MMS.

A sample of SF was measured using the CF-MMS (Fig. 52). The measured dielectric constant agrees well with [24] and [25] between 6 and 18 GHz. Again, the crude fabrication of the CF-MMS invalidates the measured loss tangent data.

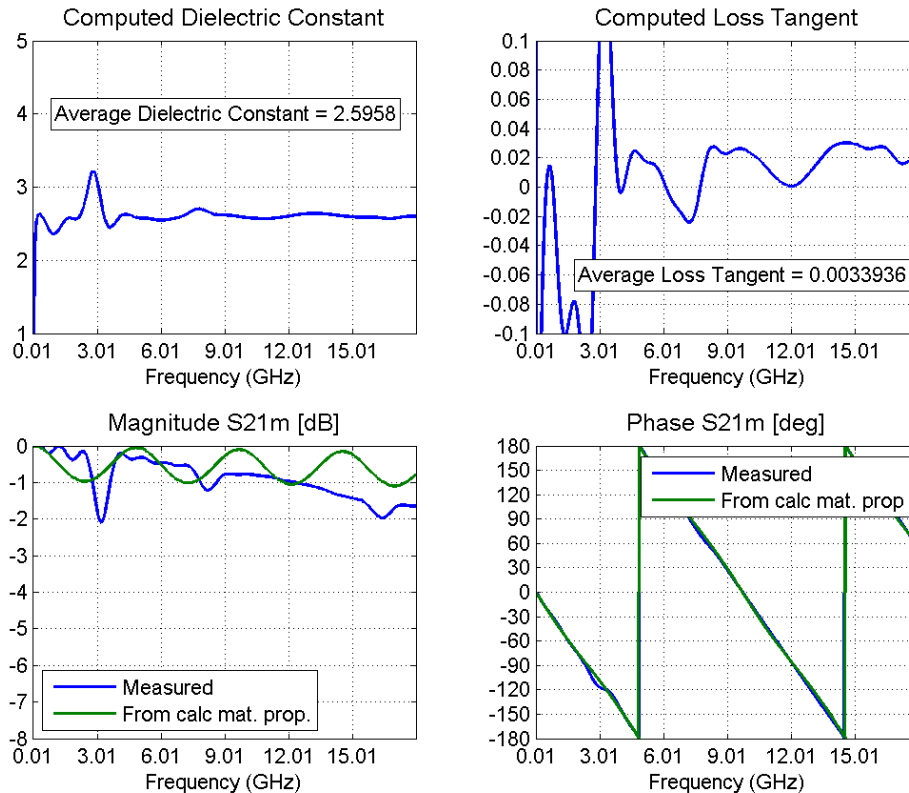


Fig. 52. SF sample measurement results using the CF-MMS.

6.8 Conclusion

The initial MMSs fabricated provided a low-cost approach to create and refine data processing routines. Accurate dielectric constants were computed for the FS-MSS at X-band and for the CF-MMS between 6 and 18 GHz. Crude fabrication employed in the CF-MSS systems severely affected the measurement of loss tangents. The FS-MMS calculated an acceptable average loss tangent for the large Plexiglas sample; however, material samples are often available in small coupons only. The accuracy of the measured complex permittivity depends on the accuracy employed by of the measurement technique.

CHAPTER VII

FUTURE WORK AND CONCLUSION

7.1 A Tunable Two-Pole Chebyshev SIW Filter

A tunable two-pole Chebyshev SIW filter design by coupling two tunable SIW resonators provides more desirable passband characteristics (Fig. 53). The width of the coupling window controls the coupling between the two tunable resonators.

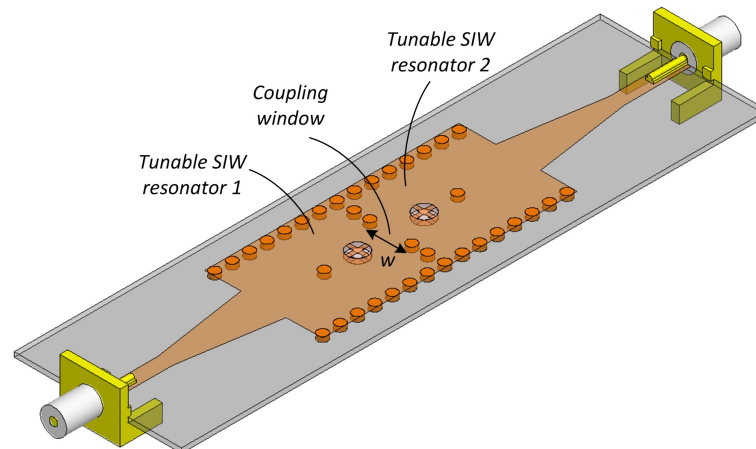


Fig. 53. A Two-pole tunable SIW Chebyshev filter.

Early simulations show the achievement of a true Chebyshev response. Across reconfiguration, with the initial low-loss estimates for ε_1 and ε_2 , the Chebyshev response falters. The external coupling to the tunable resonator may need to be modified to confine the fields in the resonator improving the filter performance across reconfiguration. When simulated with the new estimates for ε_1 and ε_2 , the RL decreases

and IL increase more significantly since dissipation occurs from two resonators as opposed to only one. Low-loss dispersions are necessary for this filter design.

7.2 Possible 3rd SIW Tunable Resonator Design Iterations

The current tunable SIW resonator achieves $\Delta f_{0,g} = 12.1\%$ reconfiguration with a RL > 8 dB and IL < 6 dB utilizing the current dispersions up to $g \leq 0.3$. Attempts at improving the RL and IL performance and maintain $\Delta f_{0,g} = 12.1\%$ utilizing the current high-loss dispersions up to $g \leq 0.5$ are shown in Fig. 54. The design in a) repositions the dielectric post in the SIW resonator to weaken the perturbation, possibly lowering the losses while maintaining $\Delta f_{0,g} \geq 12.1\%$. The design in b) redefines the cavity to provide a stronger resonance and decreases the volume of the dielectric post to weaken the perturbation. The combination of stronger resonance and weaker perturbation could possibly lower the losses while maintaining $\Delta f_{0,g} \geq 12.1\%$. The design in c) positions smaller dielectric post around the center of the SIW resonator where the fields are strongest. This weakens the perturbation (possibly lowering the losses) of each post; however, the increase in the number of posts may provide sufficient frequency shift. The design in d) sandwiches a smaller dielectric post between two copper plates. Physically the copper plates could be composed of metal tubing with a small inner diameter. The current developed on the copper plates strengthen the electric fields between them, increasing the perturbations effect. The overall volume of the fluidic dispersion decreases from the addition of the metal plates possibly decreasing the losses.

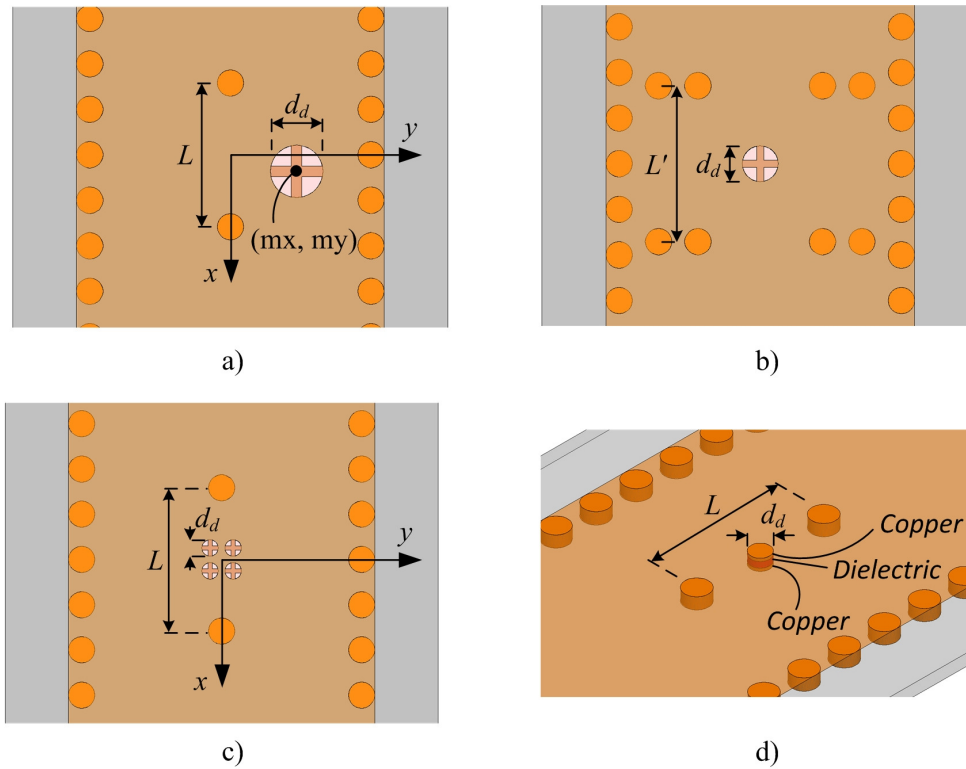


Fig. 54. Attempts at possible 3rd tunable SIW resonator design iterations.

All the possible design iterations in Fig. 54 are currently unable to increase performance utilizing $\vartheta \leq 0.5$. The reason becomes evident by rearranging (3.20) to

$$2 \left(\frac{\varepsilon_d''}{\varepsilon_d' - \varepsilon} \right) = C = \frac{1}{Q} \left(\frac{\omega}{\omega_0 - \omega} \right), \quad (6.10)$$

with $Q_0 = \infty$. Decreasing the Q of a given material perturbation requires the frequency shift to decrease in order for (6.10) to be satisfied. The designs in Fig. 54 all attempted to increase Q while maintaining $\omega_0 - \omega$; however, the physics of (6.10) are difficult to fight.

7.3 Advancements to MMS

The FS-MSS can be used to measure liquid samples by creating a liquid sample holder from the Plexiglas material [28]. The Plexiglas sections can be effectively removed from the measurement by finding the equivalent $ABCD$ parameters of the measured S parameters (A_m, B_m, C_m, D_m) and applying

$$\begin{bmatrix} A_{MUT} & B_{MUT} \\ C_{MUT} & D_{MUT} \end{bmatrix} = \begin{bmatrix} A_p & B_p \\ C_p & D_p \end{bmatrix}^{-1} \begin{bmatrix} A_m & B_m \\ C_m & D_m \end{bmatrix} \begin{bmatrix} A_p & B_p \\ C_p & D_p \end{bmatrix}^{-1} \quad (6.11)$$

The $ABCD$ matrix for the MUT can be converted back to S parameters and used to compute the complex dielectric constant using the processing techniques in Chapter IV. For large samples, an acceptable average loss tangent can be computed on the FS-MMS. Therefore, the liquid sample holder in place with the FS-MMS may accurately compute the loss tangent of SF and the fluidic dispersions.

7.4 Final Conclusion

In this work a tunable SIW resonator was analyzed, designed, and tested. Reconfiguration was employed via a dielectric post containing a fluidic dispersion, variable dielectric material based on the volume fraction \mathcal{G} of the particle in the dispersions. Accurate circuit modeling and closed-form expression predict the performance of the resonator well without utilizing full-wave simulations. Over two design iterations, it was found that the fluidic dispersions intrinsically possessed much higher losses than expected deteriorating the tunable SIW resonator performance. New estimates for the fluidic dispersion were discovered by comparing simulated data from a parametric study to measured data. Although the high-loss fluidic dispersions currently

hinder the performance of the tunable SIW resonator, utilizing low-loss fluidic dispersions would greatly increase the resonator performance across reconfiguration. The development of systems tailored for material characterization would expand research efforts to finding low-loss fluidic dispersions. Two initial material measurement systems were developed to measure the complex permittivity of solid and liquid samples. Initial testing showed very large samples are necessary to accurately measure the dielectric constant and loss tangent of a solid sample on the FS-MMS. The CF-MMS can accurately measure the dielectric constant of a liquid sample but the accuracy suffers from crude fabrication techniques when measuring losses. The two MMS provided an initial step in the development of more advanced systems.

REFERENCES

- [1] J.-S. Hong, *Microstrip filters for RF microwave applications*. New York, NY: Wiley, 2001.
- [2] D. M. Pozar, *Microwave engineering*. Hoboken, NJ: J. Wiley, 2005.
- [3] D. Deslandes and K. Wu, "Integrated microstrip and rectangular waveguide in planar form," *Microwave and Wireless Components Letters, IEEE*, vol. 11, pp. 68-70, 2001.
- [4] D. Deslandes and K. Wu, "Design consideration and performance analysis of substrate integrated waveguide components," in *Microwave Conference, 2002. 32nd European*, 2002, pp. 1-4.
- [5] D. Deslandes and W. Ke, "Single-substrate integration technique of planar circuits and waveguide filters," *Microwave Theory and Techniques, IEEE Transactions on*, vol. 51, pp. 593-596, 2003.
- [6] C. Xiao-Ping, W. Ke and D. Drolet, "Substrate integrated waveguide filter with improved stopband performance for satellite ground terminal," *Microwave Theory and Techniques, IEEE Transactions on*, vol. 57, pp. 674-683, 2009.
- [7] C. Xiao-Ping, W. Ke and L. Zhao-Long, "Dual-band and triple-band substrate integrated waveguide filters with chebyshev and quasi-elliptic responses," *Microwave Theory and Techniques, IEEE Transactions on*, vol. 55, pp. 2569-2578, 2007.
- [8] L. S. Nagurney, "Software defined radio in the electrical and computer engineering curriculum," in *Frontiers in Education Conference, 2009. FIE '09. 39th IEEE*, 2009, pp. 1-6.
- [9] R. Berezdivin, R. Breinig and R. Topp, "Next-generation wireless communications concepts and technologies," *Communications Magazine, IEEE*, vol. 40, pp. 108-116, 2002.
- [10] M. Xiaoyu, Y. Kawano, O. Toyoda, T. Suzuki, S. Ueda *et al.*, "Miniaturized microwave tunable bandpass filters on high-k LTCC," in *Microwave Conference Proceedings (APMC), 2010 Asia-Pacific*, 2010, pp. 139-142.

- [11] A. Abbaspour-Tamijani, L. Dussopt and G. M. Rebeiz, "Miniature and tunable filters using MEMS capacitors," *Microwave Theory and Techniques, IEEE Transactions on*, vol. 51, pp. 1878-1885, 2003.
- [12] I. Reines, P. Sang-June and G. M. Rebeiz, "Compact low-loss tunable X-band bandstop filter with miniature RF-MEMS switches," *Microwave Theory and Techniques, IEEE Transactions on*, vol. 58, pp. 1887-1895, 2010.
- [13] V. Sekar, M. Armendariz and K. Entesari, "A 1.2 -1.6-GHz substrate-integrated-waveguide RF MEMS tunable filter," *Microwave Theory and Techniques, IEEE Transactions on*, vol. 59, pp. 866-876, 2011.
- [14] F. Drummond and G. H. Huff, "Reconfiguration and thermoregulation using biologically inspired vascular networks," in *Antennas and Propagation (EUCAP), Proceedings of the 5th European Conference on*, 2011, pp. 3668-3669.
- [15] G. H. Huff and S. Goldberger, "A coaxial stub microfluidic impedance transformer "COSMIX"," *Microwave and Wireless Components Letters, IEEE*, vol. 20, pp. 154-156, 2010.
- [16] S. A. Long and G. H. Huff, "Experiments on a fluidic loading mechanism for beam-steering reflectarrays," in *Wireless Information Technology and Systems (ICWITS), 2010 IEEE International Conference on*, 2010, pp. 1-4.
- [17] X. Feng and W. Ke, "Guided-wave and leakage characteristics of substrate integrated waveguide," *Microwave Theory and Techniques, IEEE Transactions on*, vol. 53, pp. 66-73, 2005.
- [18] F. Ishihara and S. Iiguchi, "Equivalent characteristic impedance formula of waveguide and its applications," *Electronics and Communications in Japan (Part II: Electronics)*, vol. 75, pp. 54-66, 1992.
- [19] J. E. Rayas-Sanchez, "An improved EM-based design procedure for single-layer substrate integrated waveguide interconnects with microstrip transitions," in *Signal Integrity and High-Speed Interconnects, 2009. IMWS 2009. IEEE MTT-S International Microwave Workshop Series on*, 2009, pp. 27-30.
- [20] R. F. Harrington, *Time-harmonic electromagnetic fields*. New York: IEEE Press : Wiley-Interscience, 2001.

- [21] A. H. Sihvola, *Electromagnetic mixing formulas and applications*. London: Institution of Electrical Engineers, 1999.
- [22] N. Marcuvitz, *Waveguide handbook*. London, UK: P. Peregrinus on behalf of the Institution of Electrical Engineers, 1986.
- [23] Ansoft, "HFSS v12.0," Pittsburg, PA, 2009.
- [24] A. R. Von Hippel, *Dielectric materials and applications; papers by twenty-two contributors*. Cambridge, New York: published jointly by the Technology Press of M.I.T. and Wiley, 1954.
- [25] N. Tiercelin, P. Coquet, R. Sauleau, V. Senez and H. Fujita, "Polydimethylsiloxane membranes for millimeter-wave planar ultra flexible antennas," *Journal of micromechanics and microengineering : structures, devices, and systems.*, vol. 16, pp. 2389-2395, 2006.
- [26] Agilent, "Free Space Materials Measurement Seminar," 2005.
- [27] A. M. Nicolson and G. F. Ross, "Measurement of the intrinsic properties of materials by time-domain techniques," *Instrumentation and Measurement, IEEE Transactions on*, vol. 19, pp. 377-382, 1970.
- [28] M. A. B. Aris, D. K. Ghodgaonkar and N. Khadri, "Nondestructive and noncontact dielectric measurement methods for low-loss liquids using free space microwave measurement system in 8 - 12.5 GHz frequency range," in *RF and Microwave Conference, 2004. RFM 2004. Proceedings*, 2004, pp. 182-189.

APPENDIX A
MULLER'S METHOD

Muller's method is an iterative root-finding method which fits three initial points to a second-degree polynomial (p_2). The root of p_2 is found from the quadratic formula and used as an improved estimate in the next iteration of initial points. Begin by considering some general function $f(x)$ shown in Fig. A1.

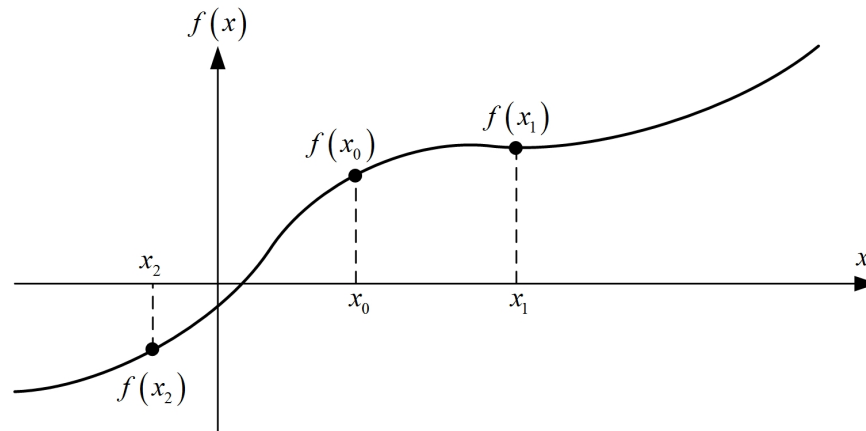


Fig. A1. General $f(x)$

Three initial guess are required x_2, x_0, x_1 (in increasing order) where the function is evaluated to be $f(x_2) = f_2, f(x_0) = f_0$, and $f(x_1) = f_1$, respectively. It is convenient to use the transformation $v = x - x_0$ so that the vertical axis passes through x_0 . Then we can define $h_1 = x_1 - x_0$ and $h_2 = x_0 - x_2$. A second degree polynomial p_2 can be constructed which passes through f_2, f_0 , and f_1 as seen in Fig. A2.

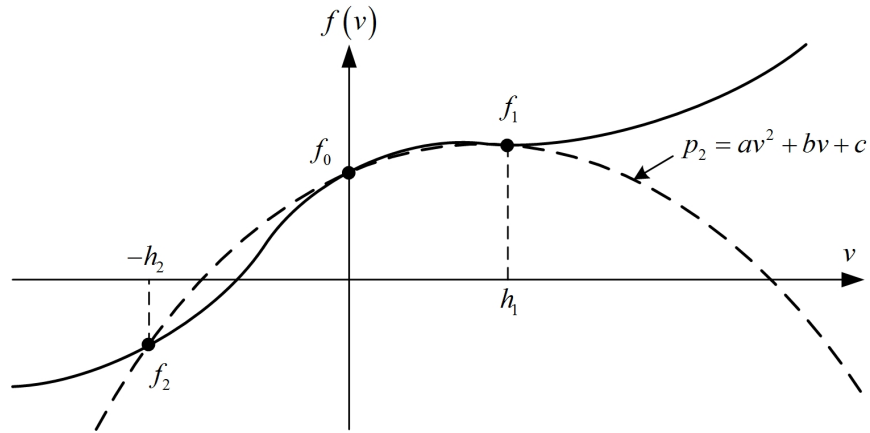


Fig. A2. General $f(x)$ with fitted polynomial p_2

The polynomial p_2 can be constructed as follows.

$$f(v=0) = a(0)^2 + b(0) + c = f_0 \quad (\text{A1.1})$$

$$f(v=h_1) = a(h_1)^2 + b(h_1) + c = f_1 \quad (\text{A1.2})$$

$$f(v=-h_2) = a(h_2)^2 - b(h_2) + c = f_2 \quad (\text{A1.3})$$

From (A1.1),

$$c = f_0. \quad (\text{A1.4})$$

Thus,

$$a(h_1)^2 + b(h_1) + f_0 = f_1 \quad (\text{A1.5})$$

$$a(h_2)^2 - b(h_2) + f_0 = f_2. \quad (\text{A1.6})$$

From (A1.5),

$$b = \frac{f_1 - f_0 - ah_1^2}{h_1}. \quad (\text{A1.7})$$

Substituting (A1.7) into (A1.6) and defining $\gamma = \frac{h_2}{h_1}$ yields,

$$a = \frac{f_1\gamma - f_0(1+\gamma) + f_2}{\gamma h_1^2(1+\gamma)}. \quad (\text{A1.8})$$

The root of the p_2 can be computed from an alternative form of the quadratic formula,

$$v = \frac{-b \pm \sqrt{b^2 - 4ac}}{2a} \left(\frac{-b \mp \sqrt{b^2 - 4ac}}{-b \mp \sqrt{b^2 - 4ac}} \right) = \frac{-2c}{b \pm \sqrt{b^2 - 4ac}} \quad (\text{A1.9})$$

The alternative form of the quadratic formula in (A1.9) can reduce loss of precision in the numerical evaluation of the roots. The loss of precision in the conventional form occurs when b is very close the value of the square root term in the numerator. In the alternative form if b is very close to the square root term, the precision does not suffer since the denominator (and not the numerator) is affected. The root of the non-transformed second-degree polynomial is then

$$x_r = x_0 - \frac{2c}{b \pm \sqrt{b^2 - 4ac}} \quad (\text{A1.10})$$

Equation (A1.10) produces two possible roots. The root which is closest to x_0 is chosen. In the next iteration the root x_r becomes one the three initial points. If x_r is larger than x_0 , then the next iterations will use x_0 , x_r , and x_1 as the initial values (in increasing order, i.e., $x_{2,i+1} = x_0$, $x_{0,i+1} = x_r$, $x_{1,i+1} = x_1$). If x_r is smaller than x_0 , then the next iterations will use x_2 , x_r , and x_0 as the initial values (in increasing order, i.e., $x_{2,i+1} = x_1$, $x_{0,i+1} = x_r$, $x_{1,i+1} = x_0$). This is iterated until $f(x_r) < (\text{tolerance value})$. The analysis is valid for complex roots so long as complex arithmetic is used.

APPENDIX B

MATLAB MMS DATA PROCESSING CODE

The main function is:

```

clear all; close all; clc;
%% User inputs
% specify the data file location and name
fid_base = 'some directory'; % input directory
fid_output = 'some directory'; % output directory
fname = 'filename.cti';

er_g = x(1-jy); % complex dielectric constant guess
d_in = d; % sample thickness (inch)

type = 0; % measurement type (1 for freespace, 0 for coax)

%% Constants
e0 = (10^-9)/(36*pi); % permittivity in a vac
u0 = (4*pi)*10^-7; % permeability in a vac
inch2meter = 0.0254; % inches to meters conversion

%% Read in data (CTI file)
file = [fid_base,fname]; % concatenate file
data = read_cti(file); % read cti file and store in data in 'data'

%% Compute Complex Dielectric Constant
for i=1:length(data.freq_Hz)
    S21m = data.S21.re(i)+j*data.S21.im(i); % measured S21
    if type == 1
        lam0=(1/sqrt(e0*u0))/data.freq_Hz(i); % free-space wavelength
        S21m_shift_ref(i) = exp(-j*pi*d_in*inch2meter/lam0)*...
            S21m*exp(-j*pi*d_in*inch2meter/lam0);...
            % shift the reference plane to MUT faces
        temp = ...
            Muller_Method(er_g,d_in,data.freq_Hz(i),S21m_shift_ref(i));
            % compute the complex er using Muller's method
    else
        temp = Muller_Method(er_g,d_in,data.freq_Hz(i),S21m);
            % compute the complex er using Muller's method
    end
    result.comp_er(i) = temp.comp_er; % store complex er
    result.iteration(i) = temp.iterations; % store # of iterations
end

% average dielectric constant and loss tangent over freq range
result.avg_er = mean(real(result.comp_er));
result.avg_tand = mean(-imag(result.comp_er)./real(result.comp_er));

```

```

%% Computed response from calculated material properties
S21_calc =...
    expected_S21(result.avg_er,result.avg_tand,d_in,data.freq_Hz);
S21_calc_dB = 20*log10(abs(S21_calc));
S21_calc_phs_deg = atan2(imag(S21_calc),real(S21_calc))*180/pi;

%% Plot It
figure
subplot(2,2,1)
plot(data.freq_GHz,real(result.comp_er),'Linewidth',1.5); grid on;
title('Computed Dielectric Constant','FontSize',12)
xlabel('Frequency (GHz)')
axis([data.freq_GHz(1) data.freq_GHz(length(data.freq_GHz)) 1 5])
set(gca,'xtick',
[data.freq_GHz(1):3:data.freq_GHz(length(data.freq_GHz))])
set(gca,'ytick',[1:1:5])
text(1,4,['Average Dielectric Constant = ',
num2str(result.avg_er),'],'BackgroundColor','white','Edgecolor','black')

subplot(2,2,2)
plot(data.freq_GHz,-
imag(result.comp_er)./real(result.comp_er),'Linewidth',1.5); grid on
title('Computed Loss Tangent','FontSize',12)
xlabel('Frequency (GHz)')
axis([data.freq_GHz(1) data.freq_GHz(length(data.freq_GHz)) -0.1 0.1])
set(gca,'xtick',
[data.freq_GHz(1):3:data.freq_GHz(length(data.freq_GHz))])
set(gca,'ytick',[-0.1:0.02:0.1])
text(2,-0.06,['Average Loss Tangent = ',
num2str(result.avg_tand),'],'BackgroundColor','white','Edgecolor','black')

subplot(2,2,3)
plot(data.freq_GHz,data.S21.mag_dB,data.freq_GHz,S21_calc_dB,'Linewidth',
1.5); grid on;
legend('Measured','From calc mat. prop.','Location','SouthWest')
title('Magnitude S21m [dB]','FontSize',12)
xlabel('Frequency (GHz)')
axis([data.freq_GHz(1) data.freq_GHz(length(data.freq_GHz)) -8 0])
set(gca,'xtick',
[data.freq_GHz(1):3:data.freq_GHz(length(data.freq_GHz))])
set(gca,'ytick',[-8:1:0])

% subplot(2,2,4)
%
plot(data.freq_GHz,data.S21.phs_deg,data.freq_GHz,S21_calc_phs_deg,data
.freq_GHz,180/pi*angle(S21m_shift_ref),'Linewidth',1.5); grid on
% legend('Measured','From calc mat. prop','Meas w/Shift in Ref
Plane','Location','SouthEast')
% title('Phase S21m [deg]','FontSize',12)
% xlabel('Frequency (GHz)')

```

```

% axis([data.freq_GHz(1) data.freq_GHz(length(data.freq_GHz)) -180
180])
% set(gca,'xtick',
[data.freq_GHz(1):1:data.freq_GHz(length(data.freq_GHz))])
% set(gca,'ytick', [-180:30:180])

subplot(2,2,4)
plot(data.freq_GHz,data.S21.phs_deg,data.freq_GHz,S21_calc_phs_deg,'Lin
ewidth',1.5); grid on
legend('Measured','From calc mat. prop','Location','NorthEast')
title('Phase S21m [deg]','FontSize',12)
xlabel('Frequency (GHz)')
axis([data.freq_GHz(1) data.freq_GHz(length(data.freq_GHz)) -180 180])
set(gca,'xtick',
[data.freq_GHz(1):3:data.freq_GHz(length(data.freq_GHz))])
set(gca,'ytick', [-180:30:180])

%% Save data
fout = [fid_output,fname(1:length(fname)-4)]; % concatenate output file
saveas(gcf,[fout,'.png'],'png') % save file as PNG

```

The following code compute Muller's Method on (6.8):

```

function [data] = Muller_Method(er_g, d_in, freq_Hz, S21m)

%% Constants
inch2meter = 0.0254; % inches to meters conversion
e0 = (10^-9)/(36*pi); % permittivity in a vac
u0 = (4*pi)*10^-7; % permeability in a vac
eta0 = sqrt(u0/e0); % free-space wave impedance

%% ----- Muller's Method -----
x2(1) = er_g-er_g*0.5; % second initial point (< than guess)
x0(1) = er_g; % guess point
x1(1) = er_g+er_g*0.5; % third initial point (> than guess)
Er = 1; % initialize function to pass 1st iteration
i=1; % initialize iteration

while(abs(Er) > 1e-10)

    % evaluate E = S21c-S21m at three initial points
    f2 = S21_E(x2(i),freq_Hz,d_in*inch2meter,S21m);
    f0 = S21_E(x0(i),freq_Hz,d_in*inch2meter,S21m);
    f1 = S21_E(x1(i),freq_Hz,d_in*inch2meter,S21m);

    % transform the axes to pass through x0 (v = x-x0)
    h1 = x1(i)-x0(i); % x1 transformed
    h2 = x0(i)-x2(i); % x2 transformed
    y = h2/h1; % gamma

```

```

% compute second-order polynomial coefficients
c = f0;
a = (y*f1 - f0*(1+y) + f2)/(y*h1^2*(1+y));
b = (f1 - f0 - a*h1^2)/h1;

% compute roots from the quadratic formula and choose the root
% which is closer to x0
xr1(i) = x0(i) - 2*c/(b+sqrt(b^2-4*a*c));
xr2(i) = x0(i) - 2*c/(b-sqrt(b^2-4*a*c));

if abs(xr1(i)-x0(i)) < abs(xr2(i)-x0(i))
    xr(i) = xr1(i); % if |xr1|-|x0| < |xr2|-|x0|
else
    xr(i) = xr2(i); % if |xr1|-|x0| > |xr2|-|x0|
end

% determine next initial points for the next iteration and store
% them in a temporary variable
if xr(i) > x0(i)
    x2_t = x0(i);
    x0_t = xr(i);
    x1_t = x1(i);
else
    x2_t = x2(i);
    x0_t = xr(i);
    x1_t = x0(i);
end

% evaluate E=S21c-S21m at the computed root
Er(i) = S21_E(xr(i),freq_Hz,d_in*inch2meter,S21m);

% set next iteration initial points
x2(i+1) = x2_t; x0(i+1) = x0_t; x1(i+1) = x1_t;

i=i+1; % increment iteration
end

data.iterations = i-1;
data.comp_er = xr(i-1);

```

The function E is defined as follows:

```

function E = S21_E(er, freq_Hz, d_m, S21m)

e0 = (10^-9)/(36*pi); % permittivity in a vac
u0 = (4*pi)*10^-7; % permeability in a vac
eta0 = sqrt(u0/e0); % freespace wave impedance

lam0=(1/sqrt(e0*u0))./freq_Hz; % free-space wavelength

gam = j*2*pi*sqrt(er)/lam0;

```

```

T = exp(-gam*d_m);           % transmission coeffiecient through MUT
z = sqrt(1/er);             % normalized wave impedance
R = (z-1)/(z+1);           % reflection coeffienct at air-MUT

S21c = T*(1-R^2)/(1-R^2*T^2); % calculated S21

E = S21c-S21m;

```

The expected S_{21} response is computed from:

```

function S21 = expected_S21(er_p,tand,d_in,freq_Hz)

%% Constants
inch2meter = 0.0254;      % inches to meters conversion
e0 = (10^-9)/(36*pi);     % permittivity in a vac
u0 = (4*pi)*10^-7;       % permeability in a vac
eta0 = sqrt(u0/e0);      % freespace wave impedance

%% Transmission coefficient
d_m = d_in*inch2meter;
er=er_p*(1-j*tand);
lam0=(1/sqrt(e0*u0))./freq_Hz;

gam = j*2*pi*sqrt(er)./lam0;
T = exp(-gam*d_m);
z = sqrt(1/er);
R = (z-1)/(z+1);

S21 = T*(1-R^2)./(1-R^2*T.^2);

```

The CTI S parameter file is read from:

```

function [data] = read_cti(file)

%% Read in data from citi file
fo = fopen(file); % open file
line = fgetl(fo); % get the 1st line
grab_freq_data = 0; % 0 means don't grab freq; 1 means grab freq
grab_data = 0; % 0 means don't grab data; 1 means grab data

% First parse through top of file for number of data pts and which S
% parameters were measured

i=1; % start index for S parameters
while strcmp(line,'VAR_LIST_BEGIN')==0
    if strcmp(line(1:8),'VAR Freq')==1 % if line contains 'VAR Freq'
        npts = sscanf(line,'%s %s %s %u'); % find # of data points
    end
    if strcmp(line(1:4),'DATA')==1 % if line contains DATA
        sp(i,:) = sscanf(line,'%s %s %s'); % collect S parameter
    end
end

```

```

        i=i+1;                                % increment index
    end
    line = fgetl(fo);                          % next line
end

sparms = cellstr(sp);    % create array of strings from character matrix
line = fgetl(fo);      % move to next line

% Next collect all freq pts

for i=1:1:npts
    data.freq_Hz(i) = sscanf(line, '%f');
    data.freq_GHz(i) = data.freq_Hz(i)*1e-9;
    line = fgetl(fo);
end

% Next collect all S parameter data

i=1;    % start with the first S parameter in the array "sparms" above
while i<=length(sparms)

    if strcmp(line, 'BEGIN')==1;              % if line is BEGIN

        line = fgetl(fo);                    % go to next line
        if strcmp('S11', sparms(i))==1      % if S11 parameter
            for k=1:1:npts
                % collect real(S11) for all freq pts
                data.S11.re(k) = sscanf(line, '%f');
                % collect imag(S11) for all freq pts
                data.S11.im(k) = sscanf(line, '%*f,%f');
                data.S11.mag(k) = sqrt(data.S11.re(k)^2+data.S11.im(k)^2);
                data.S11.mag_dB(k) = 20*log10(data.S11.mag(k));
                data.S11.phs_rad(k) = atan2(data.S11.im(k), data.S11.re(k));
                data.S11.phs_deg(k) = data.S11.phs_rad(k)*180/pi;
                data.S11.phs_unwrap_rad =
                    pi/180*unwrap(data.S11.phs_rad*180/pi);
                data.S11.phs_unwrap_deg = unwrap(data.S11.phs_rad*180/pi);
                line = fgetl(fo);
            end
        elseif strcmp('S12', sparms(i))==1   % if S12 parameter
            for k=1:1:npts
                % collect real(S12) for all freq pts
                data.S12.re(k) = sscanf(line, '%f');
                % collect imag(S12) for all freq pts
                data.S12.im(k) = sscanf(line, '%*f,%f');
                data.S12.mag(k) = sqrt(data.S12.re(k)^2+data.S12.im(k)^2);
                data.S12.mag_dB(k) = 20*log10(data.S12.mag(k));
                data.S12.phs_rad(k) = atan2(data.S12.im(k), data.S12.re(k));
                data.S12.phs_deg(k) = data.S12.phs_rad(k)*180/pi;
                data.S12.phs_unwrap_rad =
                    pi/180*unwrap(data.S12.phs_rad*180/pi);
                data.S12.phs_unwrap_deg = unwrap(data.S12.phs_rad*180/pi);
            end
        end
        i=i+1;
    end
end

```

```

        line = fgetl(fo);
    end
elseif strcmp('S21',sparms(i))==1          % if S21 parameter
    for k=1:1:npts
        % collect real(S21) for all freq pts
        data.S21.re(k) = sscanf(line, '%f');
        % collect imag(S21) for all freq pts
        data.S21.im(k) = sscanf(line, '%*f,%f');
        data.S21.mag(k) = sqrt(data.S21.re(k)^2+data.S21.im(k)^2);
        data.S21.mag_dB(k) = 20*log10(data.S21.mag(k));
        data.S21.phs_rad(k) = atan2(data.S21.im(k),data.S21.re(k));
        data.S21.phs_deg(k) = data.S21.phs_rad(k)*180/pi;
        data.S21.phs_unwrap_rad =
            pi/180*unwrap(data.S21.phs_rad*180/pi);
        data.S21.phs_unwrap_deg = unwrap(data.S21.phs_rad*180/pi);
        line = fgetl(fo);
    end
elseif strcmp('S22',sparms(i))==1          % if S22 parameter
    for k=1:1:npts
        % collect real(S22) for all freq pts
        data.S22.re(k) = sscanf(line, '%f');
        % collect imag(S22) for all freq pts
        data.S22.im(k) = sscanf(line, '%*f,%f');
        data.S22.mag(k) = sqrt(data.S22.re(k)^2+data.S22.im(k)^2);
        data.S22.mag_dB(k) = 20*log10(data.S22.mag(k));
        data.S22.phs_rad(k) = atan2(data.S22.im(k),data.S22.re(k));
        data.S22.phs_deg(k) = data.S22.phs_rad(k)*180/pi;
        data.S22.phs_unwrap_rad =
            pi/180*unwrap(data.S22.phs_rad*180/pi);
        data.S22.phs_unwrap_deg = unwrap(data.S22.phs_rad*180/pi);
        line = fgetl(fo);
    end
end
i=i+1;          % go to next S parameter in "sparms"

else          % if the line is not BEGIN
    line = fgetl(fo); % go to next line
end

end

```

VITA

Name: Joel Daniel Barrera

Address: 3128 TAMU, 214 Zachry Bldg., College Station, TX, 77843

Email Address: jdbar.tx@gmail.com

Education: B.S., Electrical Engineering, Texas A&M University, 2009
M.S., Electrical Engineering, Texas A&M University, 2011